

11. A. C. Eckbreth, *Laser Diagnostics for Combustion Temperature and Species*, Abacus Press, Cambridge, CA, 1988.
12. R. M. Measures, *J. Appl. Phys.* **39**, 5,232–5,245 (1968).
13. Flow Visualization VII: Proc. Seventh Int. Symp. Flow Visualization J. P. Crowder, ed., 1995.
14. S. W. Allison and G. T. Gillies, *Rev. Sci. Instrum.* **68**(7), 1–36 (1997).
15. K. T. V. Grattan and Z. Y. Zhang, *Fiber Optic Fluorescence Thermometry*, Chapman & Hall, London, 1995.
16. K. W. Tobin, G. J. Capps, J. D. Muhs, D. B. Smith, and M. R. Cates, *Dynamic High-Temperature Phosphor Thermometry*. Martin Marietta Energy Systems, Inc. Report No. ORNL/ATD-43, August 1990.
17. B. W. Noel, W. D. Turley, M. R. Cates, and K. W. Tobin, Two-Dimensional Temperature Mapping using Thermographic Phosphors. Los Alamos National Laboratory Technical Report No. LA_UR_90_1534, May 1990.
18. D. J. Bizzak and M. K. Chyu, *Rev. Sci. Instrum.* **65**, 102 (1994).
19. P. Goss, A. A. Smith, and M. E. Post, *Rev. Sci. Instrum.* **60**(12), 3,702–3,706 (1989).
20. R. P. Marino, B. D. Westring, G. Laufer, R. H. Krauss, and R. B. Whitehurst, *AIAA J.* **37**, 1,097–1,101 (1999).
21. A. C. Edge, G. Laufer, and R. H. Krauss, *Appl. Opt.* **39**(4), 546–553 (2000).
22. B. C. Crites, in *Measurement Techniques Lecture Series 1993–05*, von Karman Institute for Fluid Dynamics, 1993.
23. B. G. McLachlan, and J. H. Bell, *Exp. Thermal Fluid Sci.* **10**(4), 470–485 (1995).
24. T. Liu, B. Campbell, S. Burns, and J. Sullivan, *Appl. Mech. Rev.* **50**(4), 227–246 (1997).
25. J. H. Bell, E. T. Schairer, L. A. Hand, and R. Mehta, to be published in *Annu. Rev. Fluid Mech.*
26. V. Mosharov, V. Radchenko, and S. Fonov, *Luminescent Pressure Sensors in Aerodynamic Experiments*. Central Aerohydrodynamic Institute and CW 22 Corporation, Moscow, Russia, 1997.
27. M. M. Ardasheva, L. B. Nevshy, and G. E. Pervushin, *J. Appl. Mech. Tech. Phys.* **26**(4), 469–474 (1985).
28. M. Gouterman, *J. Chem. Ed.* **74**(6), 697–702 (1997).
29. J. Kavandi and J. P. Crowder, *AIAA Paper* 90-1516, 1990.
30. M. E. Sellers and J. A. Brill, *AIAA Paper* 94-2481, 1994.
31. W. Ruyten, *Rev. Sci. Instrum.* **68**(9), 3,452–3,457 (1997).
32. C. W. Fisher, M. A. Linne, N. T. Middleton, G. Fiechtner, and J. Gord, *AIAA Paper* 99-0771.
33. P. Hartmann and W. Ziegler, *Anal. Chem.* **68**, 4,512–4,514 (1996).
34. Quantitative Surface Temperature Measurement using Two-Color Thermographic Phosphors and Video Equipment, US Pat. 4,885,633 December 5, 1989 G. M. Buck.
35. G. M. Buck, *J. Spacecraft Rockets* **32**(5), 791–794 (1995).

LIDAR

P. S. ARGALL
 R. J. SICA
 The University of Western Ontario
 London, Ontario, Canada

INTRODUCTION

Light detection and ranging (lidar) is a technique in which a beam of light is used to make range-resolved remote measurements. A lidar emits a beam of light, that interacts with the medium or object under study. Some of this light is scattered back toward the lidar. The backscattered light captured by the lidar's receiver is used to determine some property or properties of the medium in which the beam propagated or the object that caused the scattering.

The lidar technique operates on the same principle as radar; in fact, it is sometimes called laser radar. The principal difference between lidar and radar is the wavelength of the radiation used. Radar uses wavelengths in the radio band whereas lidar uses light, that is usually generated by lasers in modern lidar systems. The wavelength or wavelengths of the light used by a lidar depend on the type of measurements being made and may be anywhere from the infrared through the visible and into the ultraviolet. The different wavelengths used by radar and lidar lead to the very different forms that the actual instruments take.

The major scientific use of lidar is for measuring properties of the earth's atmosphere, and the major commercial use of lidar is in aerial surveying and bathymetry (water depth measurement). Lidar is also used extensively in ocean research (1–5) and has several military applications, including chemical (6–8) and biological (9–12) agent detection. Lidar can also be used to locate, identify, and measure the speed of vehicles (13). Hunters and golfers use lidar-equipped binoculars for range finding (14,15).

Atmospheric lidar relies on the interactions, scattering, and absorption, of a beam of light with the constituents of the atmosphere. Depending on the design of the lidar, a variety of atmospheric parameters may be measured, including aerosol and cloud properties, temperature, wind velocity, and species concentration.

This article covers most aspects of lidar as it relates to atmospheric monitoring. Particular emphasis is placed on lidar system design and on the Rayleigh lidar technique. There are several excellent reviews of atmospheric lidar available, including the following:

Lidar for Atmospheric Remote Sensing (16) gives a general introduction to lidar; it derives the lidar equation for various forms of lidar including Raman and differential absorption lidar (DIAL). This work includes details of a Raman and a DIAL system operated at NASA's Goddard Space Flight Center. *Lidar Measurements: Atmospheric Constituents, Clouds, and Ground Reflectance* (17) focuses on the differential absorption and DIAL techniques as well as their application to monitoring aerosols, water vapor, and minor species in the troposphere and lower stratosphere. Descriptions of several systems are given, including the results of measurement programs using these systems. *Optical and Laser Remote Sensing* (18) is a compilation of papers that review a variety of lidar techniques and applications. *Lidar Methods and Applications* (19) gives an overview of lidar that covers all areas of atmospheric monitoring and research, and emphasizes

the role lidar has played in improving our understanding of the atmosphere. *Coherent Doppler Lidar Measurement of Winds* (20) is a tutorial and review article on the use of coherent lidar for measuring atmospheric winds. *Lidar for Atmospheric and Hydrospheric Studies* (21) describes the impact of lidar on atmospheric and to a lesser extent oceanic research particularly emphasizing work carried out during the period 1990 to 1995. This review details both the lidar technology and the environmental research and monitoring undertaken with lidar systems.

Laser Remote Sensing (22) is a comprehensive text that covers lidar. This text begins with chapters that review electromagnetic theory, which is then applied to light scattering in the atmosphere. Details, both theoretical and practical, of each of the lidar techniques are given along with many examples and references to operating systems.

HISTORICAL OVERVIEW

Syngé in 1930 (23) first proposed the method of determining atmospheric density by detecting scattering from a beam of light projected into the atmosphere. Syngé suggested a scheme where an anti-aircraft searchlight could be used as the source of the beam and a large telescope as a receiver. Ranging could be accomplished by operating in a bistatic configuration, where the source and receiver were separated by several kilometres. The receiver's field-of-view (FOV) could be scanned along the searchlight beam to obtain a height profile of the scattered light's intensity from simple geometric considerations. The light could be detected by using a photoelectric apparatus. To improve the signal level and thus increase the maximum altitude at which measurements could be made, Syngé also suggested that a large array of several hundred searchlights could be used to illuminate the same region of the sky.

The first reported results obtained using the principles of this method are those of Duclaux (24) who made a photographic recording of the scattered light from a searchlight beam. The photograph was taken at a distance of 2.4 km from the searchlight using an $f/1.5$ lens and an exposure of 1.5 hours. The beam was visible on the photograph to an altitude of 3.4 km. Hulbert (25) extended these results in 1936 by photographing a beam to an altitude of 28 km. He then made calculations of atmospheric density profiles from the measurements.

A monostatic lidar, the typical configuration for modern systems, has the transmitter and receiver at the same location, (Fig. 1). Monostatic systems can be subdivided into two categories, coaxial systems, where the laser beam is transmitted coaxially with the receiver's FOV, and biaxial systems, where the transmitter and receiver are located adjacent to each other. Bureau (26) first used a monostatic system in 1938. This system was used for determining cloud base heights. As is typical with a monostatic system, the light source was pulsed, thereby enabling the range at which the scattering occurred to be determined from the round-trip time of the scattered light pulse, as shown in Fig. 2.

By refinements of technique and improved instrumentation, including electrical recording of backscattered light

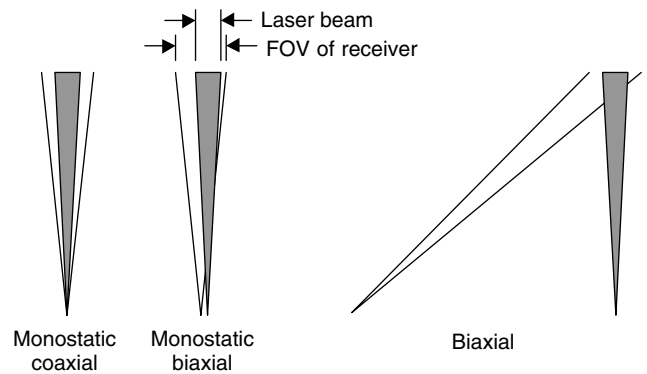


Figure 1. Field of view arrangements for lidar laser beam and detector optics .

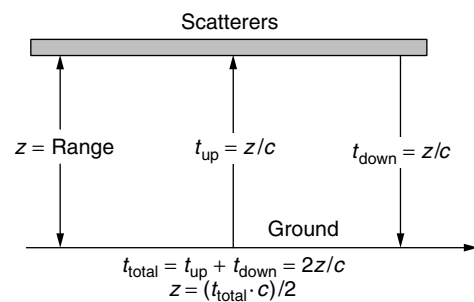


Figure 2. Schematic showing determination of lidar range.

intensity, Elterman (27) calculated density profiles up to 67.6 km. He used a bistatic system where the transmitter and receiver were 20.5 km apart. From the measured density profiles, Elterman calculated temperature profiles using the Rayleigh technique.

Friedland et al. (28) reported the first pulsed monostatic system for measuring atmospheric density in 1956. The major advantage of using a pulsed monostatic lidar is that for each light pulse fired, a complete altitude-scattering profile can be recorded, although commonly many such profiles are required to obtain measurements that have a useful signal-to-noise ratio. For a bistatic lidar, scattering can be detected only from a small layer in the atmosphere at any one time, and the detector must be moved many times to obtain an altitude profile. The realignment of the detector can be difficult due to the large separations and the strict alignment requirements of the beam and the FOV of the detector system. Monostatic lidar inherently averages the measurements at all altitudes across exactly the same period, whereas a bistatic system takes a snapshot of each layer at a different time.

The invention of the laser (29) in 1960 and the giant pulse or Q-switched laser (30) in 1962 provided a powerful new light source for lidar systems. Since the invention of the laser, developments in lidar have been closely linked to advances in laser technology. The first use of a laser in a lidar system was reported in 1962 by Smullins and Fiocco (31), who detected laser light scattered from the lunar surface using a ruby laser that fired 0.5-J pulses at 694 nm. In the following year, these same workers

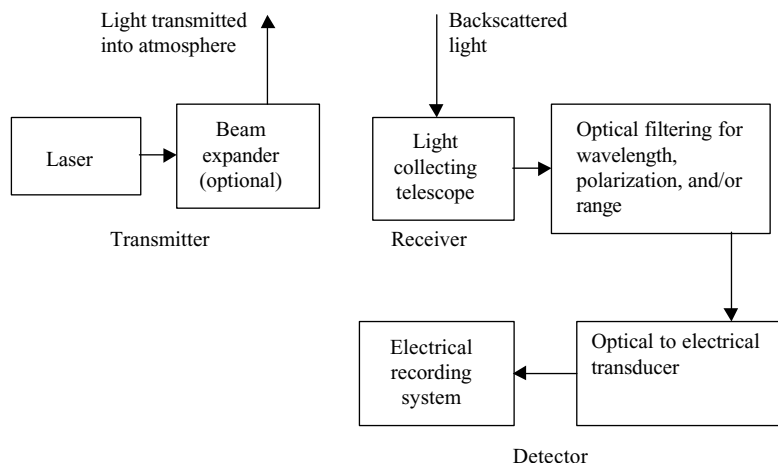


Figure 3. Block diagram of a generic lidar system.

reported the detection of atmospheric backscatter using the same laser system (32).

LIDAR BASICS

The first part of this section describes the basic hardware required for a lidar. This can be conveniently divided into three components: the transmitter, the receiver, and the detector. Each of these components is discussed in detail. Figure 3, a block diagram of a generic lidar system, shows how the individual components fit together.

In the second part of this section, the lidar equation that gives the signal strength measured by a lidar in terms of the physical characteristics of the lidar and the atmosphere is derived.

Transmitter

The purpose of the transmitter is to generate light pulses and direct them into the atmosphere. Figure 4 shows the laser beam of the University of Western Ontario's Purple Crow lidar against the night sky. Due to the special characteristics of the light they produce, pulsed lasers are ideal as sources for lidar systems. Three properties of a pulsed laser, low beam divergence, extremely narrow spectral width, and short intense pulses, provide significant advantages over white light as the source for a lidar.

Generally, it is an advantage for the detection system of a lidar to view as small an area of the sky as possible as this configuration keeps the background low. Background is light detected by the lidar that comes from sources other than the transmitted laser beam such as scattered or direct sunlight, starlight, moonlight, airglow, and scattered light of anthropogenic origin. The larger the area of the sky that the detector system views, that is, the larger the FOV, the higher the measured background. Therefore, it is usually preferable for a lidar system to view as small an area of the sky as possible. This constraint is especially true if the lidar operates in the daytime (33–35), when scattered sunlight becomes the major source of background. Generally, it is also best if the entire laser beam falls within the FOV of the detector system as



Figure 4. Laser beam transmitted from the University of Western Ontario's Purple Crow lidar. The beam is visible from several kilometers away and often attracts curious visitors. See color insert.

this configuration gives maximum system efficiency. The divergence of the laser beam should be sufficiently small, so that it remains within the FOV of the receiver system in all ranges of interest.

A simple telescope arrangement can be used to decrease the divergence of a laser beam. This also increases the diameter of the beam. Usually, only a small reduction in the divergence of a laser beam is required in a lidar system, because most lasers have very low divergence. Thus, a small telescope, called a beam expander, is usually

all that is required to obtain a sufficiently well-collimated laser beam for transmission into the atmosphere.

The narrow spectral width of the laser has been used to advantage in many different ways in different lidar systems. It allows the detection optics of a lidar to spectrally filter incoming light and thus selectively transmit photons at the laser wavelength. In practice, a narrowband interference filter is used to transmit a relatively large fraction of the scattered laser light (around 50%) while transmitting only a very small fraction of the background white light. This spectral selectivity means that the signal-to-background ratio of the measurement will be many orders of magnitude greater when a narrowband source and a detector system interference filter are used in a lidar system.

The pulsed properties of a pulsed laser make it an ideal source for a lidar, as this allows ranging to be achieved by timing the scattered signal. A white light or a continuous-wave (cw) laser can be mechanically or photo electrically chopped to provide a pulsed beam. However, the required duty cycle of the source is so low that most of the energy is wasted. To achieve ranging, the length of the laser pulses needs to be much shorter than the required range resolution, usually a few tens of meters. Therefore, the temporal length of the pulses needs to be less than about 30 ns. The pulse-repetition frequency (PRF) of the laser needs to be low enough that one pulse has time to reach a sufficient range, so that it no longer produces any signal before the next pulse is fired. This constraint implies a maximum PRF of about 20 kHz for a lidar working at close range. Commonly, much lower laser PRFs are used because decreasing the PRF reduces the active observing time of the receiver system and therefore, reduces the background. High PRF systems do have the distinct advantage of being able to be made "eye-safe" because the energy transmitted in each pulse is reduced (36).

Using the values cited for the pulse length and the PRF gives a maximum duty cycle for the light source of about 0.06%. This means that a chopped white light or cw laser used in a lidar would have effective power of less than 0.06% of its actual power. However, for some applications, it is beneficial to use cw lasers and modulation code techniques for range determination (37,38).

The type of laser used in a lidar system depends on the physical quantity that the lidar has been designed to measure. Some measurements require a very specific wavelength (i.e., resonance-fluorescence) or wavelengths (i.e., DIAL) and can require complex laser systems to produce these wavelengths, whereas other lidars can operate across a wide wavelength range (i.e., Rayleigh, Raman and aerosol lidars). The power and pulse-repetition frequency of a laser must also match the requirements of the measurements. There is often a compromise of these quantities, in addition to cost, in choosing from the types of lasers available.

Receiver

The receiver system of a lidar collects and processes the scattered laser light and then directs it onto a photodetector, a device that converts the light to an electrical signal. The primary optic is the optical element

that collects the light scattered back from the atmosphere and focuses it to a smaller spot. The size of the primary optic is an important factor in determining the effectiveness of a lidar system. A larger primary optic collects a larger fraction of the scattered light and thus increases the signal measured by the lidar. The size of the primary optic used in a lidar system may vary from about 10 cm up to a few meters in diameter. Smaller aperture optics are used in lidar systems that are designed to work at close range, for example, a few 100 meters. Larger aperture primary optics are used in lidar systems that are designed to probe the middle and upper regions of the Earth's atmosphere where the returned signal is a much smaller fraction of the transmitted signal (39,40). Smaller primary optics may be lenses or mirrors; the larger optics are typically mirrors. Traditional parabolic glass telescope primary mirrors more than about a half meter in diameter are quite expensive, and so, some alternatives have been successfully used with lidar systems. These alternatives include liquid-mirror telescopes (LMTs) (36,41) (Fig. 5), holographic elements (42,43), and multiple smaller mirrors (44–46).

After collection by the primary optic, the light is usually processed in some way before it is directed to the detector system. This processing can be based on wavelength, polarization, and/or range, depending on the purpose for which the lidar has been designed.

The simplest form of spectral filtering uses a narrowband interference filter that is tuned to the laser wavelength. This significantly reduces the background, as described in the previous section, and blocks extraneous signals. A narrowband interference filter that is typically around 1 nm wide provides sufficient rejection of background light for a lidar to operate at nighttime. For daytime use, a much narrower filter is usually employed (47–49). Complex spectral filtering schemes



Figure 5. Photograph of the 2.65-m diameter liquid mercury mirror used at the University of Western Ontario's, Purple Crow lidar. See color insert.

are often used for Doppler and high-spectral-resolution lidar (50–54).

Signal separation based on polarization is a technique that is often used in studying atmospheric aerosols, including clouds, by using lidar systems (55–58). Light from a polarized laser beam backscattered by aerosols will generally undergo a degree of depolarization, that is, the backscattered light will not be plane polarized. The degree of depolarization depends on a number of factors, including the anisotropy of the scattering aerosols. Depolarization of backscattered light also results from multiple scattering of photons.

Processing of the backscattered light based on range is usually performed in order to protect the detector from the intense near-field returns of higher power lidar systems. Exposing a photomultiplier tube (PMT) to a bright source such as a near-field return, even for a very short time, produces signal-induced noise (SIN) that affects the ability of the detection system to record any subsequent signal accurately (59,60). This protection is usually achieved either by a mechanical or electrooptical chopper that closes the optical path to the detector during and immediately after the laser fires or by switching the detector off during this time, called gating.

A mechanical chopper used for protecting the detector is usually a metal disk that has teeth on its periphery and is rotated at high speed. The laser and chopper are synchronized so that light backscattered from the near field is blocked by the chopper teeth but light scattered from longer ranges is transmitted through the spaces between the teeth. The opening time of the chopper depends on both the diameter of the optical beam that is being chopped and the speed at which the teeth move. Generally, opening times around 20–50 ms corresponding to a lidar range of between a few and several kilometers are required. Opening times of this order can be achieved by using a beam diameter of a few millimeters and a 10-cm diameter chopper rotating at several thousand revolutions per minute (61).

Signal Detection and Recording

The signal detection and recording section of a lidar takes the light from the receiver system and produces a permanent record of the measured intensity as a function of altitude. The signal detection and recording system in the first lidar experiments was a camera and photographic film (24,25).

Today, the detection and recording of light intensity is done electronically. The detector converts the light into an electrical signal, and the recorder is an electronic device or devices, that process and record this electrical signal.

Photomultiplier tubes (PMTs) are generally used as detectors for incoherent lidar systems that use visible and UV light. PMTs convert an incident photon into an electrical current pulse (62) large enough to be detected by sensitive electronics. Other possibilities for detectors (63) for lidar systems include multianode PMTs (64), MCPs (65), avalanche photodiodes (66,67), and CCDs (68,69). Coherent detection is covered in a later section.

The output of a PMT has the form of current pulses that are produced both by photons entering the PMT and the thermal emission of electrons inside the PMT. The output due to these thermal emissions is called dark current.

The output of a PMT can be recorded electronically in two ways. In the first technique, photon counting, the pulses are individually counted; in the second technique, analog detection, the average current due to the pulses is measured and recorded. The most appropriate method for recording PMT output depends on the rate at which the PMT produces output pulses, which is proportional to the intensity of the light incident on the PMT. If the average rate at which the PMT produces output pulses is much less than the average pulse width, then individual pulses can be easily identified, and photon counting is the more appropriate recording method.

Photon Counting

Photon counting is a two-step process. First, the output of the PMT is filtered using a discriminator to remove a substantial number of the dark counts. This is possible because the average amplitude of PMT pulses produced by incident photons is higher than the average amplitude of the pulses produced by dark counts. A discriminator is essentially a high-speed comparator whose output changes state when the signal from the PMT exceeds a preset level, called the discriminator level. By setting the discriminator level somewhere between the average amplitude of the signal count and dark count levels, the discriminator can effectively filter out most of the dark counts. Details of operating a photomultiplier in this manner can be found in texts on optoelectronics (62,70,71).

The second step in photon counting involves using a multichannel counter, often called a multichannel scaler (MCS). A MCS has numerous memory locations that are accessed sequentially and for a fixed time after the MCS receives a signal indicating that a laser pulse has been fired into the atmosphere. If the output from the discriminator indicates that a count should be registered, then the MCS adds one to the number in the currently active memory location. In this way, the MCS can count scattered laser photons as a function of range. An MCS is generally configured to add together the signals detected from a number of laser pulses. The total signal recorded by the MCS, across the averaging period of interest, is then stored on a computer. All of the MCS memory locations are then reset to zero, and the counting process is restarted.

If a PMT produces two pulses that are separated by less than the width of a pulse, they are not resolved, and the output of the discriminator indicates that only one pulse was detected. This effect is called pulse pileup. As the intensity of the measured light increases, the average count rate increases, pulse pileup becomes more likely, and more counts are missed. The loss of counts due to pulse pileup can be corrected (39,72), as long as the count rate does not become excessive. In extreme cases, many pulses pileup, and the output of the PMT remains above the discriminator level, so that no pulses are counted.

Analog Detection

Analog detection is appropriate when the average count rate approaches the pulse-pair resolution of the detector system, usually of the order of 10 to 100 MHz depending on the PMT type, the speed of the discriminator, and the MCS. Analog detection uses a fast analog-to-digital converter to convert the average current from the PMT into digital form suitable for recording and manipulation on a computer (73).

Previously, we described a method for protecting a PMT from intense near-field returns using a rotating chopper. An alternative method for protecting a PMT is called blanking or gating (74–76). During gating, the PMT is effectively turned off by changing the distribution of voltages on the PMT's dynode chain. PMT gating is simpler to implement and more reliable than a mechanical chopper system because it has no moving parts. However, it can cause unpredictable results because gating can cause gain variations and a variable background that complicates the interpretation of the lidar returns.

Coherent Detection

Coherent detection is used in a class of lidar systems designed for velocity measurement. This detection technique mixes the backscattered laser light with light from a local oscillator in a photomixer (77). The output of the photomixer is a radio-frequency (RF) signal whose frequency is the difference between the frequencies of the two optical signals. Standard RF techniques are then used to measure and record this signal. The frequency of the measured RF signal can be used to determine the Doppler shift of the scattered laser light, which in turn allows calculation of the wind velocity (78–82).

Coherent lidar systems have special requirements for laser pulse length and frequency stability. The advantage of coherent detection for wind measurements is that the instrumentation is generally simpler and more robust than that required for incoherent optical interferometric detection of Doppler shifts (20).

An Example of a Lidar Detection System

Many lidar systems detect light at multiple wavelengths and/or at different polarization angles. The Purple Crow lidar (39,83) at the University of Western Ontario detects scattering at four wavelengths (Fig. 6). A Nd:YAG laser operating at the second-harmonic frequency (532 nm) provides the light source for the Rayleigh (532 nm) and the two Raman shifted channels, N₂ (607 nm) and H₂O (660 nm). The fourth channel is a sodium resonance-fluorescence channel that operates at 589 nm. Dichroic mirrors are used to separate light collected by the parabolic mirror into these four channels before the returns are filtered by narrowband interference filters and imaged onto the PMTs.

A rotating chopper is incorporated into the two high-signal-level channels, Rayleigh and sodium, to protect the PMTs from intense near-field returns. The chopper operates at a high speed, 8,400 rpm, and is comprised of a rotating disk that has two teeth on the outside edge. This chopper blocks all scatter from below 20 km

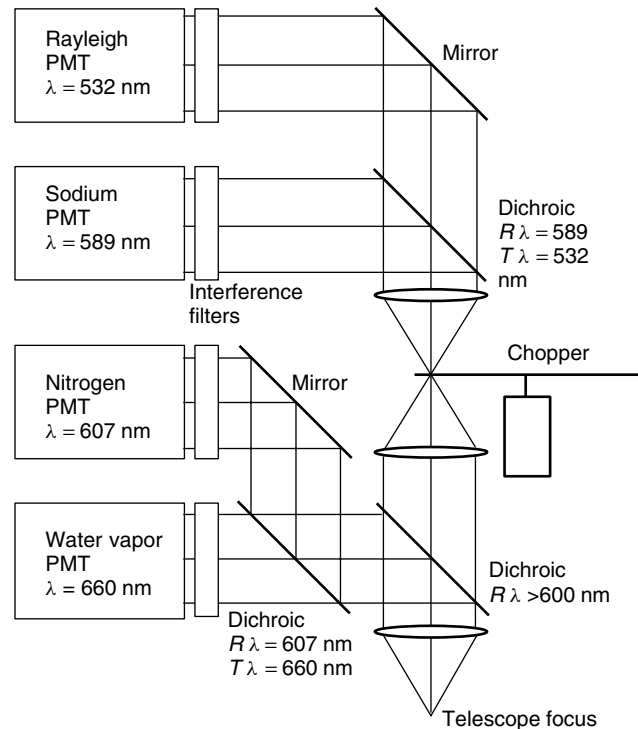


Figure 6. Schematic of the detection system of the Purple Crow lidar at the University of Western Ontario.

and is fully open by 30 km. The signal levels in the two Raman channels are sufficiently small that the PMTs do not require protection from near-field returns.

The two Raman channels are used for detecting H₂O and N₂ in the troposphere and stratosphere and thus allow measurement of water vapor concentration and temperature profiles. Measurements from the Rayleigh and sodium channels are combined to provide temperature profiles from 30 to 110 km.

THE LIDAR EQUATION

The lidar equation is used to determine the signal level detected by a particular lidar system. The basic lidar equation takes into account all forms of scattering and can be used to calculate the signal strength for all types of lidar, except those that employ coherent detection. In this section, we derive a simplified form of the lidar equation that is appropriate for monostatic lidar without any high-spectral resolution components. This equation is applicable to simple Rayleigh, vibrational Raman, and DIAL systems. It is not appropriate for Doppler or pure rotational Raman lidar, because it does not include the required spectral dependencies.

Let us define P as the total number of photons emitted by the laser in a single laser pulse at the laser wavelength λ_l and τ_t as the transmission coefficient of the lidar transmitter optics. Then the total number of photons transmitted into the atmosphere by a lidar system in a single laser pulse is given by

$$P\tau_t(\lambda_l). \quad (1)$$

The number of photons available to be scattered in the range interval r to $r + dr$ from the lidar is

$$P\tau_t(\lambda_l)\tau_a(r, \lambda_l) dr, \quad (2)$$

where $\tau_a(r, \lambda_l)$ is the optical transmission of the atmosphere at the laser wavelength, along the laser path to the range r . Note that range and altitude are equivalent only for a vertically pointing lidar.

The number of photons backscattered, per unit solid angle due to scattering of type i , from the range interval R_1 to R_2 , is

$$P\tau_t(\lambda_l) \int_{R_1}^{R_2} \tau_a(r, \lambda_l) \sigma_\pi^i(\lambda_l) N^i(r) dr, \quad (3)$$

where $\sigma_\pi^i(\lambda_l)$ is the backscatter cross section for scattering of type i at the laser wavelength and $N^i(r)$ is the number density of scattering centers that cause scattering of type i at range r .

Range resolution is most simply and accurately achieved if the length of the laser pulse is much shorter than the length of the range bins. If this condition cannot be met, the signal can be deconvolved to obtain the required range resolution (84,85). The effectiveness of this deconvolution depends on a number of factors, including the ratio of the laser pulse length to the length of the range bins, the rate at which the signal changes over the range bins, and the signal-to-noise ratio of the measurements.

The number of photons incident on the collecting optic of the lidar due to scattering of type i is

$$P\tau_t(\lambda_l)A \int_{R_1}^{R_2} \frac{1}{r^2} \tau_a(r, \lambda_l) \tau_a(r, \lambda_s) \zeta(r) \sigma_\pi^i(\lambda_l) N^i(r) dr, \quad (4)$$

where A is the area of the collecting optic, λ_s is the wavelength of the scattered light, and $\zeta(r)$ is the overlap factor that takes into account the intensity distribution across the laser beam and the physical overlap of the transmitted laser beam and the FOV of the receiver optics. The term $1/r^2$ arises in Eq. (4) due to the decreasing illuminance of the telescope by the scattered light, as the range increases.

For photon counting, the number of photons detected as pulses at the photomultiplier output per laser pulse is

$$P\tau_t(\lambda_l)A\tau_r(\lambda_s)Q(\lambda_s) \int_{R_1}^{R_2} \frac{1}{r^2} \tau_a(r, \lambda_l) \tau_a(r, \lambda_s) \zeta(r) \sigma_\pi^i(\lambda_l) N^i(r) dr, \quad (5)$$

where $\tau_r(\lambda_s)$ is the transmission coefficient of the reception optics at λ_s and $Q(\lambda_s)$ is the quantum efficiency of the photomultiplier at wavelength λ_s .

For analog detection, the current recorded can be determined by replacing the quantum efficiency of the photomultiplier $Q(\lambda_s)$ by the gain $G(\lambda_s)$ of the photomultiplier combined with the gain of any amplifiers used.

In many cases, approximations allow simplification of Eq. (5). For example, if none of the range-dependent

terms, $\tau_a(r, \lambda_l)$, $\tau_a(r, \lambda_s)$, $N^i(r)$, and $\zeta(r)$, varies significantly throughout individual range bins, then the range integral may be removed, and Eq. 5 becomes

$$P\tau_t(\lambda_l)A\tau_r(\lambda_s)Q(\lambda_s)\tau_a(R, \lambda_l)\tau_a(R, \lambda_s)\frac{1}{R^2}\zeta(R)\sigma_\pi^i(\lambda_l)N^i(R)\delta R \quad (6)$$

where R is the range of the center of the scattering volume and $\delta R = R_2 - R_1$, is the length of the range bin.

This form of the lidar equation can be used to calculate the signal strength for Rayleigh, vibrational Raman lidar, and DIAL as long as the system does not incorporate any filter whose spectral width is of the same order or smaller than the width of the laser output or the Doppler broadening function. For high-resolution spectral lidar, where a narrow-spectral-width filter or tunable laser is used, the variations in the individual terms of Eq. (6) with wavelength need to be considered. To calculate the measurement precision of a lidar that measures the Doppler shift and broadening of the laser line for wind and temperature determination, computer simulation of the instrument may be necessary.

LIGHT SCATTERING IN THE ATMOSPHERE AND ITS APPLICATION TO LIDAR

The effect of light scattering in the Earth's atmosphere, such as blue skies, red sunsets, and black, grey, and white clouds, is easily observed and reasonably well understood (86–89). Light propagating through the atmosphere is scattered and absorbed by the molecules and aerosols, including clouds that form the atmosphere. Molecular scattering takes place via a number of different processes and may be either elastic, where there is no exchange of energy with the molecule, or inelastic, where an exchange of energy occurs with the molecule. It is possible to calculate, by at least a reasonable degree of accuracy, the parameters that describe these molecular scattering processes.

The theory of light scattering and absorption by spherical aerosols, usually called Mie (90) theory, is well understood, though the application of Mie theory to lidar can be difficult in practice. This difficulty arises due to computational limits encountered when trying to solve atmospheric scattering problems where the variations in size, shape, and refractive index of the aerosol particles can be enormous (91–97). However, because aerosol lidars can measure average properties of aerosols directly, they play an important role in advancing our understanding of the effect of aerosols on visibility (98–101) as well as on climate (102,103).

Molecules scatter light by a variety of processes; there is, however, an even greater variety of terms used to describe these processes. In addition, researchers in different fields have applied the same terms to different processes. Perhaps the most confused term is Rayleigh scattering, which has been used to identify at least three different spectral regions of light scattered by molecules (104–106).

RAYLEIGH SCATTER AND LIDAR

Rayleigh theory describes the scattering of light by particles that are small compared to the wavelength of the incident radiation. This theory was developed by Lord Rayleigh (107,108) to explain the color, intensity distribution, and polarization of the sky in terms of scattering by atmospheric molecules.

In his original work on light scattering, Rayleigh used simple dimensional arguments to arrive at his well-known equation. In later years, Rayleigh (109,110) and others (22,87,111,112) replaced these dimensional arguments with a more rigorous mathematical derivation of the theory. Considering a dielectric sphere of radius r in a parallel beam of linearly polarized electromagnetic radiation, one can derive the scattering equation. The incident radiation causes the sphere to become an oscillating dipole that generates its own electromagnetic field, that is, the scattered radiation. For this derivation to be valid, it is necessary for the incident field to be almost uniform across the volume of the scattering center. This assumption leads to the restriction of Rayleigh theory to scattering by particles that are small compared to the wavelength of the incident radiation. It can be shown (113) that when $r < 0.03\lambda$, the differences between results obtained with Rayleigh theory and the more general Mie (90) theory are less than 1%.

Rayleigh theory gives the following equation for the scattered intensity from a linearly polarized beam by a single molecule:

$$I_m(\phi) = E_0^2 \frac{9\pi^2 \epsilon_0 c}{2N^2 \lambda^4} \left(\frac{n^2 - 1}{n^2 + 2} \right)^2 \sin^2 \phi, \quad (7)$$

where r is the radius of the sphere, n is the index of refractive of the sphere relative to that of the medium, that is, $n = n_{\text{molecule}}/n_{\text{medium}}$, N is the number density of the scattering centers, ϕ is the angle between the dipole axis and the scattering direction, and E_0 is the maximum value of the electrical field strength of the incident wave (22,87). From Eq. (7), we see that the intensity of the scattered light varies as λ^{-4} . However, because the refractive index may also have a small wavelength dependence, the scattered intensity is in fact not exactly proportional to λ^{-4} . Middleton (114) gives a value of $\lambda^{-4.08}$ for wavelengths in the visible.

A useful quantity in discussion is the differential-scattering cross section (22), which is also called the angular scattering cross section (87). The differential-scattering cross section is the fraction of the power of the incident radiation that is scattered, per unit solid angle, in the direction of interest. The differential-scattering cross section is defined by

$$\frac{d\sigma(\phi)}{d\Omega} I_0 = I(\phi), \quad (8)$$

where $I_0 = 1/2c\epsilon_0 E_0^2$ is the irradiance of the incident beam.

By substituting Eq. (7) in (8), it can be seen that the differential scattering cross section for an individual

molecule illuminated by plane polarized light, is

$$\frac{d\sigma_m(\phi)}{d\Omega} = \frac{9\pi^2}{N^2 \lambda^4} \left(\frac{n^2 - 1}{n^2 + 2} \right)^2 \sin^2 \phi. \quad (9)$$

If we assume that $n \approx 1$, then Eq. (9) can be approximated as

$$\frac{d\sigma_m(\phi)}{d\Omega} = \frac{\pi^2 (n^2 - 1)^2}{N^2 \lambda^4} \sin^2 \phi. \quad (10)$$

For a gas, the term $(n^2 - 1)$ is approximately proportional to the number density N (115), so Eq. (10) has only a very slight dependence on N . For air, the ratio $(n^2 - 1)/N$ varies less than 0.05% in the range of N between 0 and 65 km in altitude.

When Rayleigh theory is extended to include unpolarized light, the angle ϕ no longer has any meaning because the dipole axis may lie along any line in the plane perpendicular to the direction of propagation. The only directions that can be uniquely defined are the direction of propagation of the incident beam and the direction in which the scattered radiation is detected; we define θ as the angle between these two directions. The differential-scattering cross section for an individual molecule that is illuminated by a parallel beam of unpolarized light is

$$\frac{d\sigma_m(\theta)}{d\Omega} = \frac{\pi^2 (n^2 - 1)^2}{2N^2 \lambda^4} (1 + \cos^2 \theta). \quad (11)$$

Figure 7 shows the intensity distribution for Rayleigh scattered light from an unpolarized beam. The distribution has peaks in the forward and backward directions, and the light scattered at right angles to the incident beam is plane polarized. Because of the anisotropy of molecules, which moves the molecules dipole moment slightly out of alignment with the incident field, scattering by molecules causes some depolarization of the scattered light. This results in some light whose a polarization is parallel to the incident beam being detected at a scattering angle of 90° .

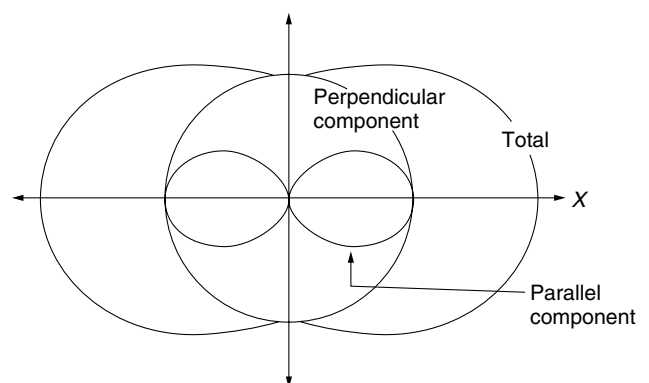


Figure 7. Intensity distribution pattern for Rayleigh scatter from an unpolarized beam traveling in the x direction. The perpendicular component refers to scattering of radiation whose electric vector is perpendicular to the plane formed by the direction of propagation of the incident beam and the direction of observation.

The depolarization ratio δ_n^t is defined as

$$\delta_n^t = \frac{I_{\parallel}}{I_{\perp}}, \quad (12)$$

where the parallel and perpendicular directions are taken with respect to the direction of the incident beam. The subscript n denotes natural (unpolarized) incident light and the superscript t denotes total molecular scattering. The depolarization is sometimes defined in terms of polarized incident light and/or for different spectral components of molecular scattering. There is much confusion about which is the correct depolarization to use under different circumstances, a fact evident in the literature. The reader should take great care to understand the terminology used by each author.

Young (104) gives a brief survey of depolarization measurements for dry air and concludes that the effective value of δ_n^t is 0.0279. He also gives a correction factor for the Rayleigh differential-scattering cross section, which, when applied to Eq. (11) gives

$$\frac{d\sigma_m(\theta)}{d\Omega} = \frac{\pi^2(n^2 - 1)^2}{2N^2\lambda^4} \frac{1 + \delta_n^t + (1 - \delta_n^t)\cos^2\theta}{1 - \left(\frac{7}{6}\right)\delta_n^t} \quad (13)$$

Most lidar applications work with direct backscatter, i.e. $\theta = \pi$, and the differential-backscatter cross section per molecule for scattering from an unpolarized beam is

$$\frac{d\sigma_m(\theta = \pi)}{d\Omega} = \frac{\pi^2(n^2 - 1)^2}{2N^2\lambda^4} \left(\frac{12}{6 - 7\delta_n^t} \right) \quad (14)$$

The correction factor for backscatter is independent of the polarization state of the incident beam (111). This means that the correction factor and thus, the backscatter cross section per molecule are independent of the polarization characteristics of the laser used in a backscatter lidar.

The Rayleigh molecular-backscatter cross section for an altitude less than 90 km and without the correction factor is given by Kent and Wright (116) as $4.60 \times 10^{-57}/\lambda^4 \text{ m}^2 \text{ sr}^{-1}$. When the correction factor is applied, with $\delta_n^t = 0.0279$, this result becomes

$$\frac{d\sigma_m(\theta = \pi)}{d\Omega} = \frac{4.75 \times 10^{-57}}{\lambda^4} \text{ m}^2 \text{ sr}^{-1} \quad (15)$$

Collis et al. (117) gives a value of the constant in Eq. (15) as $4.99 \times 10^{-57} \text{ m}^6 \text{ sr}^{-1}$.

Fiocco (118) writes Eq. (15) in the form

$$\frac{d\sigma_m(\theta = \pi)}{d\Omega} = \frac{4.73 \times 10^{-57}}{\lambda^{4.09}} \text{ m}^2 \text{ sr}^{-1} \quad (16)$$

Here, the wavelength exponent takes into account dispersion in air. Equations (15) and (16) are applicable to the atmosphere at altitudes less than 90 km. Above this altitude, the concentration of atomic oxygen becomes significant and changes the composition and thus, the refractive index. Equations (15) and (16), used in conjunction with the lidar equation [Eq. (6)] can be used

to determine the backscatter intensity of a particular Rayleigh lidar.

Rayleigh Lidar

Rayleigh lidar is the name given to the class of lidar systems that measure the intensity of the Rayleigh backscatter from an altitude of about 30 km up to around 100 km. The measured backscatter intensity can be used to determine a relative density profile; this profile is used to determine an absolute temperature profile. Rayleigh scattering is by far the dominant scattering mechanism for light above an altitude of about 30 km, except in the rare case where noctilucent clouds exist. At altitudes below about 25–30 km, light is elastically scattered by aerosols in addition to molecules. Only by using high-spectral-resolution techniques can the scattering from these two sources be separated (119). Thus, most Rayleigh lidar systems cannot be used to determine temperatures below the top of the stratospheric aerosol layer. The maximum altitude of the stratospheric aerosol layer varies with the season and is particularly perturbed after major volcanic activity.

Above about 90 km, changes in composition, due mainly to the increasing concentration of atomic oxygen, cause the Rayleigh backscatter cross-section and the mean molecular mass of air to change with altitude. This leads to errors in the temperatures derived by using the Rayleigh technique that range from a fraction of a degree at 90 km to a few degrees at 110 km. For current Rayleigh systems, the magnitude of this error is significantly smaller than the uncertainties from other sources, such as the photocount statistics, in this altitude range. Low photocount rates give rise to large statistical uncertainties in the derived temperatures at the very top of Rayleigh lidar temperature profiles (Fig. 8a). Additional uncertainties in the temperature retrieval algorithm, due to the estimate of the pressure at the top of the density profile which is required to initiate temperature integration (120), can be significant and are difficult to quantify.

The operating principle of a Rayleigh lidar system is simple. A pulse of laser light is fired up into the atmosphere, and any photons that are backscattered and collected by the receiving system are counted as a function of range. The lidar equation [Eq. (6)] can be directly applied to a Rayleigh lidar system to calculate the expected signal strength. This equation can be expressed in the form

$$\text{Signal strength} = K \left(\frac{1}{R^2} \right) N_a \delta R \quad (17)$$

where K is the product of all of the terms that can be considered constants between 30 and 100 km in Eq. (6) and N_a is the number density of air. This result assumes that there is insignificant attenuation of the laser beam as it propagates from 30 to 100 km, that is, the atmospheric transmission $\tau_a(r, \lambda_1)$ is a constant for $30 < r < 100$ km. If there are no aerosols in this region of the atmosphere and the laser wavelength is far from the absorption lines of any molecules, then the only attenuation of the laser beam is due to Rayleigh scatter and possibly

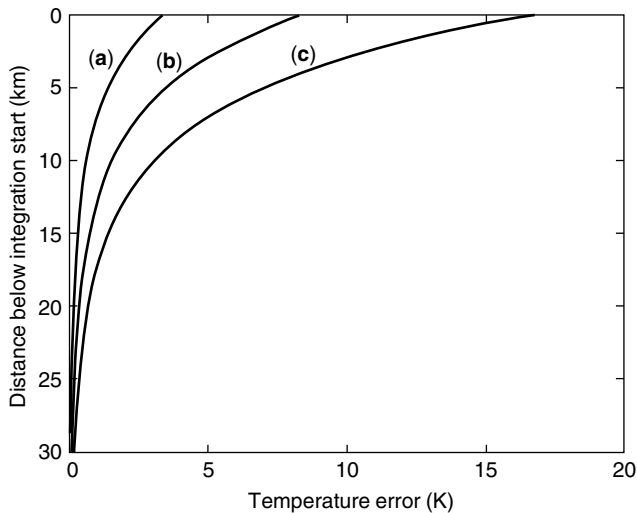


Figure 8. The propagation of the error in the calculated temperature caused by a (a) 2%, (b) 5% and (c) 10% error in the initial estimate of the pressure.

ozone absorption. Using Rayleigh theory, it can be shown that the transmission of the atmosphere from 30 to 100 km is greater than 99.99% in the visible region of the spectrum.

Equation (17) shows that after a correction for range R , the measured Rayleigh lidar signal between 30 and 100 km is proportional to the atmospheric density. K cannot be determined due to the uncertainties in atmospheric transmission and instrumental parameters [see Eq. (6)]. Hence, Rayleigh lidar can typically determine only relative density profiles. A measured relative density profile can be scaled to a coincident radiosonde measurement or model density profile, either at a single altitude or across an extended altitude range.

This relative density profile can be used to determine an absolute temperature profile by assuming that the atmosphere is in hydrostatic equilibrium and applying the ideal gas law. Details of the calculation and an error analysis for this technique can be found in both Chanin and Hauchecorne (120) and Shibata (121). The assumption of hydrostatic equilibrium, the balance of the upward force of pressure and the downward force of gravity, can be violated at times in the middle atmosphere due to instability generated by atmospheric waves, particularly gravity waves (122,123). However, sufficient averaging in space (e.g., 1 to 3 km) and in time (e.g., hours) minimizes such effects.

Calculating an absolute temperature profile begins by calculating a pressure profile. The first step in this process is to determine the pressure at the highest altitude range-bin of the measured relative density profile. Typically, this pressure is obtained from a model atmosphere. Then, using the density in the top range-bin, the pressure at the bottom of this bin is determined using hydrostatic equilibrium. This integration is repeated for the second to top density range-bin and so on down to the bottom of the density profile. Because atmospheric density increases as altitude decreases, the choice of pressure at the top range-bin becomes less significant in the calculated pressures, as the

integration proceeds. A pressure profile calculated in this way is a relative profile because the density profile from which it was determined is a relative profile. However, the ratio of the relative densities to the actual atmospheric densities will be exactly the same as the ratio of the relative pressures to the actual atmospheric pressures:

$$N_{\text{rel}} = K'N_{\text{act}}$$

and

$$P_{\text{rel}} = K'P_{\text{act}}, \quad (18)$$

where N_{rel} is the relative density and N_{act} is the actual atmospheric density, similarly for the pressure P , and K' is the unknown proportionality constant. The ideal gas law can then be applied to the relative density and pressure profiles to yield a temperature profile. Because the relative density and relative pressure profiles have the same proportionality constant [see Eq. (18)], the constants cancel, and the calculated temperature is absolute.

The top of the temperature profile calculated in this scheme is influenced by the choice of initial pressure. Figure 8 shows the temperature error as a function of altitude for a range of pressures used to initiate the pressure integration algorithm. Users of this technique are well advised to ignore temperatures from at least the uppermost 8 km of the retrieval because the uncertainties introduced by the seed pressure estimate are not easily

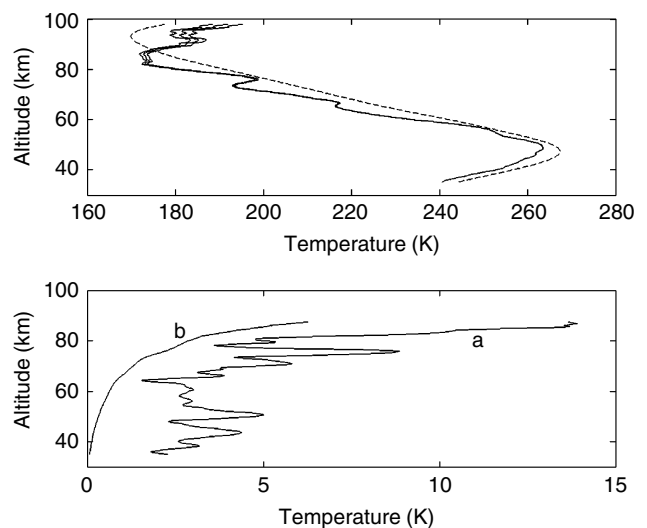


Figure 9. Top panel shows the average temperature (middle of the three solid lines) for the night of 13 August 2000 as measured by the PCL. The two outer solid lines represent the uncertainty in the temperature. Measurements are summed across 288 m in altitude and 8 hours in time. The temperature integration algorithm was initiated at 107.9 km; the top 10 km of the profile has been removed. The dashed line is the temperature from the Fleming model (289) for the appropriate location and date. Bottom panel shows (a) the rms deviation from the mean temperature profile for temperatures calculated every 15 minutes at the same vertical resolution as before. (b) is the average statistical uncertainty in the individual temperature profiles used in the calculation of the rms and is based on the photon counting statistics.

quantified, unless an independent determination of the temperature is available.

The power–aperture product is the typical measure of a lidar system’s effectiveness. The power–aperture product is the mean laser power (watts) multiplied by the collecting area of the receiver system (m^2). This result is, however, a crude metric because it ignores both the variations in Rayleigh-scatter cross section and atmospheric transmission with transmitter frequency, as well as the efficiency of the system.

The choice of a laser for use in Rayleigh lidar depends on a number of factors, including cost and ease of use. The best wavelengths for a Rayleigh lidar are in the blue–green region of the spectrum. At longer wavelengths, for example, the infrared, the scattering cross section is smaller, and thus, the return signal is reduced. At shorter wavelengths, for example, the ultraviolet, the scattering cross section is higher, but the atmospheric transmission is lower, leading to an overall reduction in signal strength. Most dedicated Rayleigh lidars use frequency-doubled Nd:YAG lasers that operate at 532 nm (green light). Other advantages of this type of laser are that it is a well-developed technology that provides a reliable, “turnkey,” light source that can produce pulses of short duration with typical average powers of 10 to 50 W. Some Rayleigh lidar systems use XeF excimer lasers that operate at about 352 nm. These systems enjoy the higher power available from these lasers, as well as a Rayleigh-scatter cross section larger than for Nd:YAG systems, but the atmospheric transmission is lower at these wavelengths. In addition, excimer lasers are generally considered more difficult and expensive to operate than Nd:YAG lasers.

An example of a temperature profile from The University of Western Ontario’s Purple Crow lidar Rayleigh (40) system is shown in Fig. 9. The top panel of the figure shows the average temperature during the night’s observations, including statistical uncertainties due to photon counting. The bottom panel shows the rms deviation of the temperatures calculated at 15-minute intervals. The rms deviations are a measure of the geophysical variations in temperature during the measurement period. Also included on the bottom panel is the average statistical uncertainty due to photon counting in the individual 15-minute profiles.

Rayleigh lidar systems have been operated at a few stations for several years building up climatological records of middle atmosphere temperature (60,124,125). The lidar group at the Service d’Aeronomie du CNRS, France has operated a Rayleigh lidar at the Observatory of Haute-Provence since 1979 (120,125–128). The data set collected by this group provides an excellent climatological record of temperatures in the middle and upper stratosphere and in the lower mesosphere.

Lidar systems designed primarily for sodium and ozone measurements have also been used as Rayleigh lidar systems for determining stratospheric and mesospheric temperatures (129–131). Rayleigh-scatter lidar measurements can be used in conjunction with independent temperature determinations to calculate molecular nitrogen and molecular oxygen mixing ratios in the mesopause region of the atmosphere (132).

Rayleigh lidar systems cannot operate when clouds obscure the middle atmosphere from their view. Most Rayleigh systems can operate only at nighttime due to the presence of scattered solar photons during the day. However, the addition of a narrow band-pass filter in the receiver optics allows daytime measurements (35,133).

Doppler Effects

Both random thermal motions and bulk-mean flow (e.g., wind) contribute to the motion of air molecules. When light is scattered by molecules, it generally undergoes a change in frequency due to the Doppler effect that is proportional to the molecules line of sight velocity. If we consider the backscattered light and the component of velocity of the scattering center in the direction of the scatter, then the Doppler shift, that is, the change in frequency $\Delta\nu$ of the laser light is given by (134)

$$\Delta\nu = \nu' - \nu \approx 2\nu \frac{v}{c} \quad (19)$$

where ν is the frequency of the incident photon, ν' is the frequency of the scattered photon, and v is the component of the velocity of the scattering center in the direction of scatter (e.g., backscatter).

The random thermal motions of the air molecules spectrally broaden the backscattered light, and radial wind causes an overall spectral shift. The velocity distribution function due to thermal motion of gas molecules in thermal equilibrium is given by Maxwell’s distribution. For a single direction component x , the probability that a molecule has velocity v_x is (135)

$$P(v_x)dv_x = \left(\frac{M}{2\pi kT}\right)^{1/2} \exp\left(-\frac{Mv_x^2}{2kT}\right) dv_x \quad (20)$$

where M is molecular weight, k is Boltzmann’s constant, T is temperature, and v_x is the component of velocity in the x direction.

Using Eqs. (19) and (20), it can be shown that when monochromatic light is backscattered by a gas, the frequency distribution of the light is given by

$$P(\nu') = \frac{1}{2\pi^{1/2}\sigma} \exp\left[-\frac{1}{2}\left(\frac{\nu' - \nu}{\sigma}\right)^2\right], \quad (21)$$

where

$$\sigma = \frac{\nu}{c} \left(\frac{2kT}{M}\right)^{1/2}. \quad (22)$$

The resulting equation for $P(\nu')$ is a Gaussian distribution whose full width at half maximum is equal to $2\sigma\sqrt{2\ln 2}$.

Equations (21) and (22) are strictly true only if all the atoms (molecules) of the gas have the same atomic (molecular) weight. However, air contains a number of molecular and atomic species, and therefore the frequency distribution function for Rayleigh backscattered light $P_a(\nu')$ is the weighted sum of Gaussian functions for each constituent. The major constituents of air, N_2 and O_2 , have similar molecular masses which allows the function $P_a(\nu')$ to be fairly well approximated by a single Gaussian

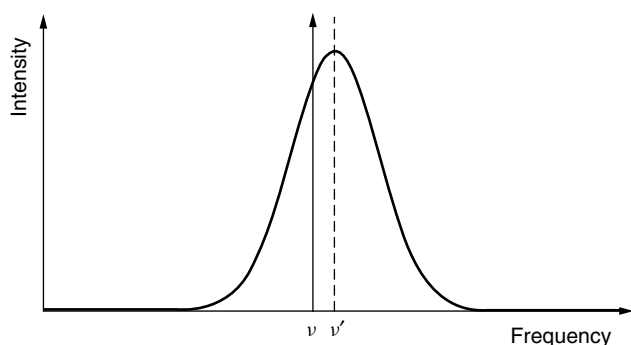


Figure 10. The frequency distribution function for Rayleigh backscattering from a clean dry atmosphere (i.e., no water vapor or aerosols), for monochromatic incident radiation of frequency ν . The broadening is due to random thermal motions and the shift is due to wind.

calculated for a gas whose a molecular mass is equal to the mean molecular mass of air.

Wind, the bulk motion of the air, causes the distribution function $P_a(\nu')$ to shift frequency while maintaining its shape. The frequency shift can be calculated directly from Eq. (19), which shows that the shift is directly proportional to the component of the wind velocity in the direction of scattering, the radial wind velocity. Figure 10 shows how the spectrum of a narrow bandwidth laser is changed due to scattering by molecules in the atmosphere.

In principle, it is possible to determine both the radial wind velocity and temperature by measuring the spectral shape of the light backscattered from air molecules in the middle atmosphere. However, using this Doppler technique, the signal-to-noise ratio requirements for temperature measurement are much higher than that for measuring winds (136), and so in practice, Rayleigh–Doppler temperature measurements are quite difficult. The advantage of this method of temperature determination is that the true kinetic temperature of the atmosphere is obtained without the need for the assumptions required by the Rayleigh technique. The group at the Observatory Haute-Provence (54,137) has demonstrated the Doppler technique for measuring middle atmosphere winds. They used a Fabry–Perot interferometer as a narrowband filter to measure the intensity of the lidar returns in a pair of wavelength ranges centered on the laser wavelength (54). Tepley et al. used a scanning interferometer to make similar measurements (136).

AEROSOL SCATTERING AND LIDAR

The theory of scattering that was developed by Mie (90) in the early 1900's is a general solution that covers the scattering of electromagnetic radiation by a homogeneous sphere for all wavelengths of radiation and spheres of all sizes and refractive indexes. A parameter that is basic to the Mie theory is the size parameter α . This parameter is a measure of the relative size of the scattering particle to the wavelength of the radiation:

$$\alpha = \frac{2\pi a}{\lambda} \quad (23)$$

where a is the radius of the scattering particle and λ is the wavelength of the incident radiation. When the particle size is small compared to the wavelength of the incident radiation (i.e., α is small), Mie theory reduces to Rayleigh theory.

Mie theory is general enough to cover the range of α 's for which Rayleigh and geometrical optics also apply, but it is mathematically more complex than Rayleigh theory and geometrical optics. This complexity has led to the common use of Mie scattering to imply scattering from particles larger than those to which Rayleigh theory applies and smaller than those to which geometrical optics applies. Mie theory solves Maxwell's equations for the boundary conditions imposed by a homogeneous sphere whose refractive index is different from that of the surrounding medium. Since Mie first published the solution to this problem, others have extended the calculations to include different shapes (e.g., infinite cylinders and paraboloids) and have provided methods for finding solutions for irregular shapes and nonhomogenous particles (112,138–140).

The atmosphere contains particles that have an infinite variety of shapes, sizes and refractive indexes. The measurement of the properties of atmospheric aerosols is also complicated by the composition and size of these particles (87,141–143). Evaporation, condensation, coagulation, absorption, desorption, and chemical reactions change the atmospheric aerosol composition on short timescales. Care must be taken with direct sampling methods that the sampling process allows correct interpretation of the properties of the aerosols collected.

Aerosol concentrations in the atmosphere vary widely with altitude, time, and location. The vertical structure of aerosol concentration profiles is complex and ever changing (144–148). There is a layer of aerosols in the atmosphere from about 15 to 23 km that is known as the stratospheric aerosol layer or the Junge (149) layer. The Junge is primarily volcanic in origin. Lidar measurements have shown that the altitude range and density of the aerosols in this layer vary widely depending on recent volcanic activity (150–154).

Extinction cross sections given by the Mie theory for size parameters corresponding to atmospheric aerosols and visible light are generally larger than extinction cross sections due to molecular scattering (87). In the atmospheric boundary layer, where the aerosol concentrations are high, the extinction of a beam of visible light is much greater than that due solely to Rayleigh scattering. Tropospheric aerosols can be a mixture of natural and anthropogenic aerosols. The effects of clouds are difficult to quantify due to the great variability they exhibit in their optical properties and in their distribution in time and space.

Atmospheric aerosols, including clouds, play an important role in the earth's radiation budget. A full understanding of the role of aerosols is important for improving weather forecasting and understanding climate change. Aerosols scatter and absorb both incoming solar radiation and outgoing terrestrial radiation. The amount of radiation that is scattered and the directions of scatter, as well as the amount of radiation absorbed, varies with aerosol

composition, size, and shape. Thus, the physical properties of aerosols determine whether they contribute net heating or cooling to the Earth's climate. Lidar provides a method of directly measuring the optical properties of atmospheric aerosol distributions and is playing an important role in current work to better quantify the atmospheric radiation budget (148,155–160).

Aerosol Lidar

Since the early 1960s, a large number of lidar systems have been built that are designed to study aerosols, including clouds, in the troposphere and lower stratosphere (161,162). Instruments using multiple wavelength transmitters and receivers (55,145,154,163–168) and polarization techniques (55,56,58,169–173) have been used to help quantify aerosol properties. A review of aerosol lidar studies is given by Reagan et al. (174). Lidars have been used to study polar stratospheric clouds (PSCs) (175–181) to help understand the role they play in ozone depletion (182–184).

In September 1994, NASA flew a space shuttle mission, STS-64, which included the LITE experiment (185–187). LITE was a technology development and validation exercise for future space lidar systems. The scientific potential of LITE was recognized early in its development, and a science steering committee was established to ensure that the scientific potential of the experiment was exploited. LITE used a Nd:YAG operating simultaneously at three frequencies, the fundamental 1,064 nm, the second harmonic 532 nm, and the third harmonic 355 nm. It also incorporated a system for automatically aligning the laser beam into the FOV of the detector system. The science objectives of LITE were to study the following atmospheric properties:

1. tropospheric aerosols, including scattering ratio and its wavelength dependence, planetary boundary layer height, structure and optical depth;
2. stratospheric aerosols, including scattering ratio and its wavelength dependence, averaged integrated backscatter, as well as stratospheric density and temperature;
3. the vertical distribution, multi layer structure, fractional cover, and optical depth of clouds;
4. the radiation budget via measurements of surface reflectance and albedo as a function of incidence angle.

Figure 11 shows a sample of the LITE measurements. This figure clearly shows regions of enhanced scatter from cloud and dust from the Saharan Desert in Northwest Africa. A worldwide correlative measurement program was undertaken for validation and intercomparison with LITE measurements. This correlative measurement program included more than 60 ground-based and several aircraft-based lidar systems (188–190).

Atmospheric aerosols have the same average velocity as atmospheric molecules; thus, the average Doppler shift of their distributions is the same, see section Doppler Effects earlier. The spectral broadening of the

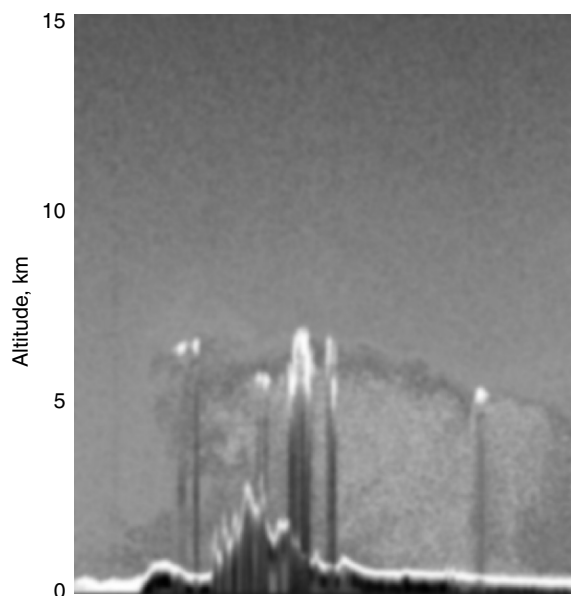


Figure 11. LITE Observations of Saharan dust, 12 September, 1994. Elevated dust layers exceeding 5 km above the Saharan Desert in Northwest Africa were observed by the Lidar In-Space Technology Experiment (LITE). The intensity plot for the 532-nm wavelength shows an aerosol layer associated with wind-blown dust from the Saharan Desert. This image is composed of individual lidar profiles sampled at 10 Hz and extends 1,000 km along the Space Shuttle Discovery orbit track during nighttime conditions. Weaker backscatter signals due to molecular backscatter are in blue, moderate backscatter signals from the dust layer are in yellow and red, and the strongest backscatter signals from clouds and the surface are in white. Opaque clouds, shown in white, prevent LITE from making observations at lower altitudes and create a shadowing effect beneath the cloud layer. The Atlas Mountain range is seen near 31°N, 6°W (David M. Winker, NASA Langley Research Center, and Kathleen A. Powell, SAIC). See color insert.

light backscattered from aerosols is much narrower than that backscattered from molecules because the mass of aerosols is much greater than that of air molecules. Light backscattered from aerosols can be separated from that backscattered from molecules using this difference in Doppler width (119,191); however, spectral separation is not necessary if only wind is to be measured because the average Doppler shift is the same for both molecular and aerosol scattering. Wind lidar using incoherent detection has been used in the troposphere (51,137); however, coherent detection techniques are more commonly used.

Coherent Doppler Lidar

Because of stronger the signal levels in the lower atmosphere, the measurement of the Doppler shift via coherent detection techniques becomes viable. Coherent Doppler lidar is used extensively in wind field mapping from the ground (192,193), from the air (194–196), and has been suggested as a possible method for global wind measurement from space platforms (194,197).

Differential Absorption Lidar (Dial)

In 1964, Schotland (198) suggested using a lidar technique now known as differential absorption lidar (DIAL). DIAL is useful for measuring the concentration of trace species in the atmosphere. The method relies on the sharp variation in optical transmission near an absorption line of the species to be detected. A DIAL transmits two closely spaced wavelengths. One of these wavelengths coincides with an absorption line of the constituent of interest, and the other is in the wing of this absorption line. During the transmission of these two wavelengths through the atmosphere, the emission that is tuned to the absorption line is attenuated more than the emission in the wing of the absorption line. The intensity of the two wavelengths that are backscattered to the DIAL instrument can then be used to determine the optical attenuation due to the species and thus, the concentration of the species. The first use of a DIAL system was for measuring atmospheric water vapor concentration (199). The DIAL technique has been extensively used for pollution monitoring (200–206). This technique is also used very successfully in the lower atmosphere for high spatiotemporal measurements of species such as NO (207), H₂O (208–210), O₃ (211–213), SO₂ (214,215), and CH₄ (216–218). Atmospheric temperature measurement is possible by the DIAL technique if the absorption line selected is temperature-dependent (219–221).

Use of the DIAL technique in the middle atmosphere has been restricted mainly to measuring ozone profiles (211,222–227). DIAL ozone measurements have extended as high as 50 km with integration times of at least a few hours required. These same lidar systems can obtain profiles up to 20 km in approximately 15 min due to the much higher ozone densities and available scatterers at the lower levels. Typically, a stratospheric ozone DIAL uses a XeCl laser that operates at 308 nm for the “on-line” or absorbed wavelength and a frequency-tripled YAG at 355 nm for the “off-line” or reference wavelength. The spectral separation between the wavelengths means that when large stratospheric aerosol loading events occurs (such as after a large volcanic eruption), the measurements become difficult to interpret due to the optical effects of the aerosols. These shortcomings have been addressed by recording the Raman-shifted backscatter from N₂ at both of the transmitted wavelengths (228).

The DIAL technique has also been used with hard targets (229,230) and is called differential optical absorption spectroscopy (DOAS). DOAS measurements are an average across the entire path from the instrument to the target, so a DOAS system is not strictly a lidar because it does not perform any ranging. DOAS has been used to monitor large areas from aircraft using the ground as the target or reflector and has been used for monitoring chemical (6–8) and biological (9–12) weapons agents.

RAMAN LIDAR

When monochromatic light, or light of sufficiently narrow spectral width, is scattered by a molecular gas or liquid, the spectrum of the scattered light, it can be observed, contains lines at wavelengths different from those of the incident radiation (231). Raman first observed this effect (232), that

is due to the interaction of radiation with the quantized vibrational and rotational energy levels of the molecule. Raman scattering involves a transfer of energy between scattered light and a molecule and is therefore, an inelastic process. The cross sections due to Raman scattering are included in the Rayleigh scattering theory (106), although Raman spectroscopists use the term Rayleigh line to indicate only the unshifted central component of the scattered light.

Each type of molecule has unique vibrational and rotational quantum energy levels and therefore, Raman scattering from each type of molecule has a unique spectral signature. This allows the identification of molecules by their scattered light spectra. Scattered radiation that loses energy during interaction with a molecule, and so decreases in frequency, is said to have a Stokes shift, whereas radiation that gains energy and increases in frequency is said to have an anti-Stokes shift. In general, Stokes radiation is more intense than anti-Stokes because the Stokes can always occur, subject to selection rules, whereas anti-Stokes also requires that the molecule is initially in an excited state.

The quantum numbers ν and J describe the vibrational and rotational states of a molecule, respectively. The Q-branch, $\Delta J = 0$, contains a number of degenerate lines leading to higher intensity for light scattered in this branch. The $\Delta\nu = +1$ frequency shifts and backscatter cross sections for a number of atmospheric molecules are given in Fig. 12. Measures (22) gives a comprehensive list of atmospheric molecules.

The pure rotational Raman spectrum (PRRS), which occurs when there is no vibrational transition, that is, $\Delta\nu = 0$, is more difficult to measure because the spectral shift of the lines is quite small. This small shift leads to technical difficulties in blocking the nearby elastic scatter from entering the detector. The PRRS of an N₂ molecule is shown in Fig. 13. The intensities of the individual lines and thus the shape of the envelope of the lines are temperature-dependent.

The term Raman lidar is generally used to refer to a lidar system that uses the Raman-shifted component where $\Delta\nu = \pm 1$, that is, a transition that involves a change in vibrational energy level. In practice the $\Delta\nu = +1$ transition is commonly used because it has higher intensity. The spectral selection of the $\Delta\nu = +1$ line in the receiver system of a lidar can be achieved by using a high-quality narrowband interference filter. It is necessary to ensure that blocking of the filter at the laser wavelength is sufficiently high that the detected elastic backscatter from molecules and aerosols is insignificant compared to Raman scattering. Generally, special order filters are required to meet this specification.

In the mid-1960s, Cooney (233) and Leonard (234) demonstrated the measurement of the Raman-shifted component of N₂ in the troposphere by lidar. The Raman lidar technique has been used most often for measuring atmospheric water vapor (34,235–240). Clouds (241–243) and aerosols (148,156,244,245) have also been studied by this technique. The use of Raman lidar is restricted to the more abundant species in the atmosphere due to the small backscatter cross section involved. The measurement of

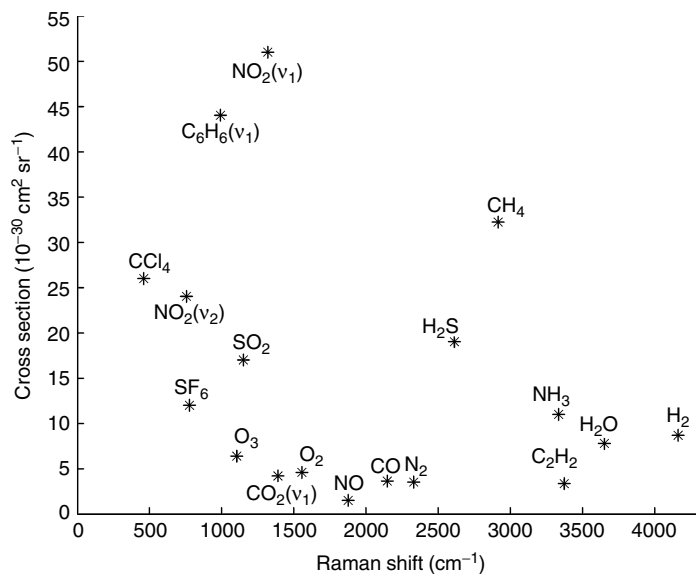


Figure 12. Vibrational Raman frequency shifts and cross sections for a number of molecules found in the atmosphere.

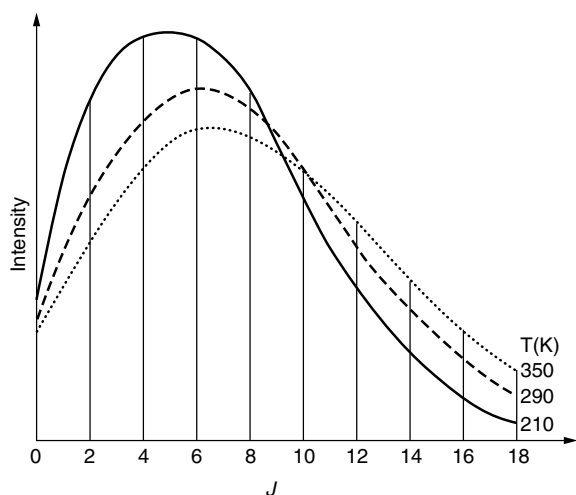


Figure 13. Intensity distribution of PRRS for N_2 at three temperatures.

atmospheric water vapor concentration by Raman lidar requires measuring the Raman backscatter from both water vapor and molecular nitrogen. The nitrogen signal is used as a reference to determine the water vapor mixing ratio from the lidar's Raman water vapor signal.

There are two methods by which Raman lidar can be used to determine atmospheric temperature. In the upper troposphere and throughout the stratosphere, the Rayleigh lidar temperature retrieval algorithm can be applied to appropriately corrected Raman N_2 measurements. Due to its spectral shift, the Raman component of the scatter from N_2 is free from the contamination of scattering from aerosols. However, aerosols affect the optical transmission of the atmosphere, an effect for which the Raman N_2 signal must be corrected before it is used for temperature calculations (246–248). Unlike Rayleigh temperature retrieval, here, the transmission is not constant with altitude. The characteristics of the background stratospheric aerosol layer are known well enough that the correction for atmospheric transmission

leads to an acceptable uncertainty in calculated temperatures. However, this correction cannot be made with sufficient accuracy lower in the atmosphere and during increased loading of the stratospheric aerosol layer.

Cooney (249) was the first to propose temperature measurement based on the shape of the PRRS for molecular nitrogen. This method uses the variation in the population of the rotational levels of a molecule with temperature; at higher temperature, the probability that a higher level is populated is greater. Figure 13 shows the envelope of the PRRS lines of a nitrogen molecule at three temperatures. Thus, temperature measurements can be made by measuring the intensity of some or all of the PRRS lines. This differential technique determines the temperature from the intensity of the Raman backscatter across a very narrow wavelength range. Changes in atmospheric transmission due to changes in aerosol properties and loading are insignificant across such a small wavelength range, making the technique almost independent of aerosols.

Separation of the central Rayleigh line from the PRRS has proved to be very difficult, even though the backscatter cross section for PRRS is much greater than that for vibrational-rotational Raman scattering. For example, for the N_2 molecule, the backscatter cross sections for vibrational, pure-rotational and elastic scattering are 3.5×10^{-30} , 1.1×10^{-28} and 3.9×10^{-27} , respectively. The spectral separation of the PRRS and the central unshifted line is quite small, and this leads to technical difficulties when trying to separate these two signals. Nevertheless, a number of Raman lidar systems have been constructed that infer temperature from rotational Raman spectra (250–255).

Resonance Lidar

Resonant scattering occurs when the energy of an incident photon is equal to the energy of an allowed transition within an atom. This is an elastic process; the atom absorbs the photon and instantly emits another photon at the same frequency. As each type of atom and molecule

has a unique absorption and hence, fluorescent spectrum, these measurements may be used to identify and measure the concentration of a particular species. A description of the theory of fluorescence and resonance can be found in both Chamberlain (256) and Measures (22).

The constant ablation of meteors in the earth's upper atmosphere leads to the existence of extended layers of alkali metals in the 80 to 115 km region (257). These metals have low abundances but very high resonant-scattering cross sections. Because resonant scattering involves an atomic transition between allowed energy levels, the probability that this process occurs is much greater than that for Rayleigh scattering. For instance, at 589 nm, the resonance-fluorescence cross section for sodium is about 10^{15} times larger than the cross section for Rayleigh scattering from air. This means that the lidar signal from 85 km measured by a sodium resonance-fluorescence lidar is about the same as the Rayleigh scatter signal measured by the same lidar at about 30 km.

Sodium. Atmospheric sodium is the most widely used of the alkali metal layers in the atmosphere because it is relatively abundant and the transmitter frequency is easy to generate. Several research groups have measured the climatology of sodium abundance, parameters related to gravity wave dynamics, temperatures, and winds (83,258–265). The sodium layer exists in the earth's atmosphere between about 80 and 105 km in altitude, a region that covers the upper part of the mesosphere and the lower part of the thermosphere. This sodium layer is sometimes referred to as the mesospheric sodium layer, although it extends well above the top of the mesosphere. The first reported use of a resonance lidar to study sodium was in 1969 (266). The existence of the mesospheric sodium layer had been known many years previous to these first lidar measurements, due to the bright, natural airglow emission that was extensively studied using passive spectroscopy (267). These passive instruments could resolve the height structure of the region only during sunrise and sunset.

The spectral shape of the sodium line at 589 nm, the D_{2a} line, is temperature-dependent and the scattering cross section is proportional to the line shape. Using this information allows the measurement of the temperature of the sodium atoms and the atmosphere surrounding them from the spectral shape of the backscattered intensity. Figure 14 shows the shape of the sodium D_{2a} line for three temperatures that are within the range of temperatures expected around the mesopause region. The sodium D_{2a} shape has been measured by lidar in a number of ways (268,269). Usually, this measurement is achieved by transmitting narrow bandwidth laser pulses at two or three well-known frequencies within the sodium D_{2a} line and recording the backscatter intensity at each of the transmitted frequencies separately. By knowing the frequency of the transmitted laser pulses and the intensity of the backscatter at each of the transmitted frequencies, the atmospheric temperature can be determined.

A technique known as Doppler-free saturation spectroscopy is used to set the frequency of the laser transmitted into the atmosphere very precisely.

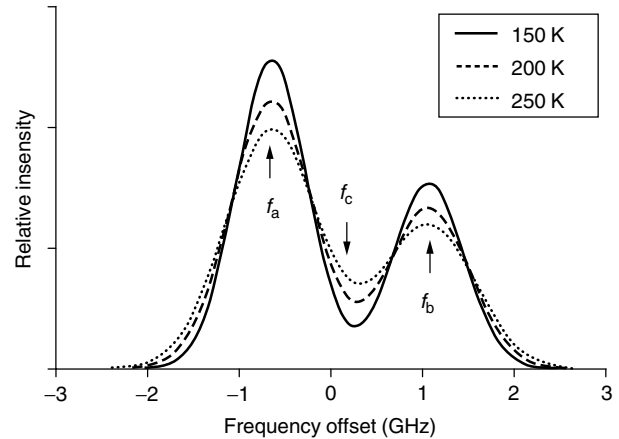


Figure 14. Shape of the sodium D_{2a} line at three temperatures.

Counterpropagating a sample of the laser output through a laboratory cell that contains sodium vapor generates the Doppler-free saturation spectrum. Under the right conditions, the fluorescence from the cell contains sharp spectral features (270) (Fig. 15). Measurements of these Doppler-free features are used in a feedback loop to control the output frequency of the laser and to lock the laser's output frequency to the frequency of the spectral feature (83,271). The Doppler-free spectrum of sodium provides three features that offer the possibility of locking the laser; f_a , f_b , and f_c . The atmospheric temperature can be determined from the ratio of the backscattered intensity at any two of three available frequencies. The pair of frequencies, which has the largest change in ratio with temperature, is f_a and f_c and so these two frequencies are commonly used. This method of temperature measurement is a direct spectral measurement and has associated errors several orders of magnitude lower than those associated with Rayleigh temperature measurements in this altitude range.

A slight drawback of this method is that it typically takes 5 to 10 seconds to switch the laser from one frequency to the other, f_a to f_c , or back again. To obtain a reasonable duty cycle, it is therefore necessary to operate the laser at each frequency for typically 30 to 60 seconds. The temperature is then determined from the ratio of measurements taken at slightly different times. The variability of the sodium and the atmosphere over this short timescale leads to some uncertainty in the temperatures measured using this technique (270).

Improvements in transmitter technology during the last decade have allowed winds as well as temperatures to be measured using narrowband sodium lidar systems (270,272,273) incorporating an acousto-optic (AO) modulator. The AO modulators are used to switch the transmitted frequency several hundred MHz to either side of a selected Doppler-free feature. This tuning enables measuring the Doppler shift and the width of the backscattered light simultaneously. Acousto-optic modulators can be turned on and off very quickly; this feature allows frequency switching between transmitted laser pulses. Typically a sodium temperature-wind lidar operates at three frequencies f_a and f_a plus and minus the AO offset. Today, such systems have been extended to a large scale, for example, the sodium lidar operated at the Starfire

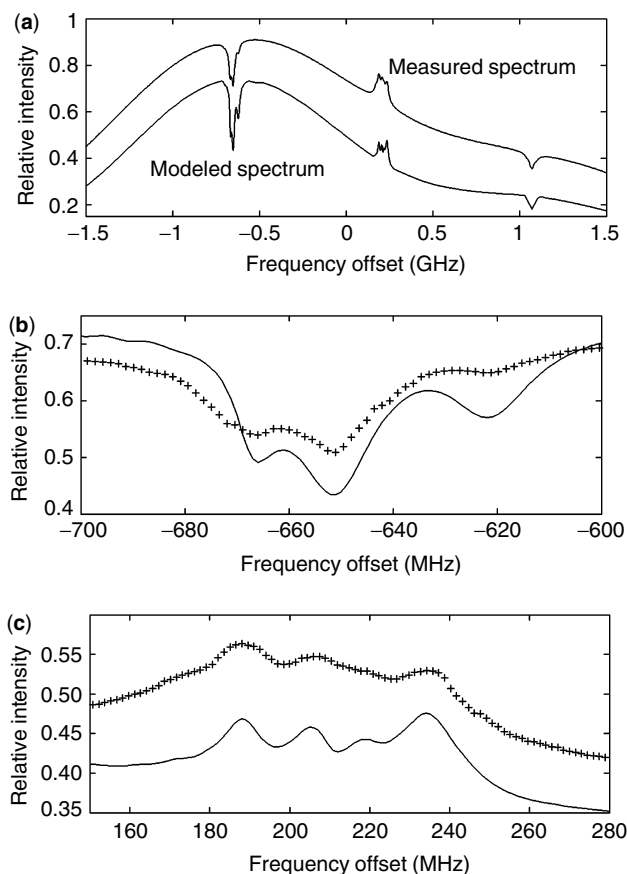


Figure 15. The Doppler-free-saturation spectra for the sodium D_{2a} line showing the locations of the spectral features f_a , f_b , and f_c . (a) D_{2a} line. (b) closeup of f_a , solid line is modeled '+'s are measured. (c) closeup of f_c .

Optical Range (SOR). Figure 16 shows an example of temperature measurements made at SOR. By simultaneously measuring temperature and vertical wind velocity, measurements at SOR have been used for the first determinations of the vertical flux of heat due to gravity waves in the mesopause region (40).

Other Metallic Species. Other alkali metals, including calcium (Ca and Ca^+) (274,275), potassium (276,277), lithium (278,279), and iron (280,281), that have resonance lines in the blue region of the visible spectrum, have also been used to study the mesopause region of the Earth's atmosphere. Thomas (282) reviews the early work in this field. Resonance lidar requires laser transmissions at the precise frequency of an absorption line of the species being studied. Traditionally, dye lasers have been used successfully to probe many of these species, though working with these dyes is difficult in the field environment. Recently, solid-state lasers have been applied to resonance lidar systems (283).

SUMMARY

Lidar has established itself as one of the most important measurements techniques for atmospheric composition

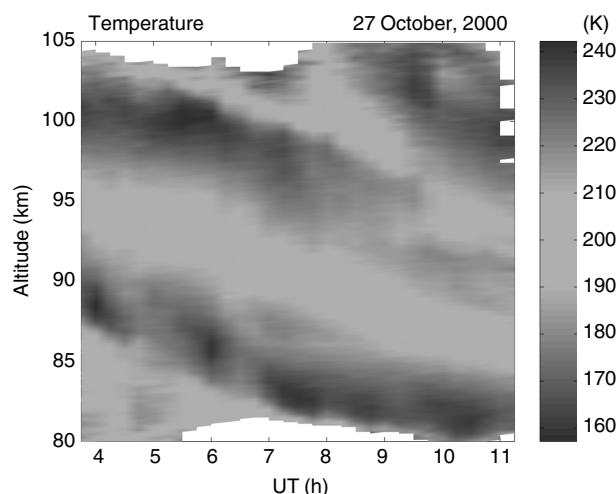


Figure 16. Temperature in the mesopause region of the atmosphere measured by the University of Illinois Sodium Wind and Temperature Lidar over the Starfire Optical Range (35.0N,106.5W), near Albuquerque, New Mexico, USA, on 27 October 2000. The local time is UT (Universal Time) 7 hours. Measurements shown in this image have been smoothed by about 0.5 hour in time and 0.5 km in altitude. The downward phase progression of the atmospheric tidal structure is clearly shown as the temperature structure move downward with time (courtesy of the University of Illinois lidar group). See color insert.

and dynamics from the surface to the upper atmosphere. It also has important uses in mapping, bathymetry, defense, oceanography and natural resource management. Lidar solutions offer themselves for a wide range of environmental monitoring problems. Except for the LITE experiment (184,185), present lidars systems are primarily located on the surface or, for campaign use, on aircraft. The next decade promises the launch of several significant space-based lidar systems to study the Earth's atmosphere. These systems include experiments to measure clouds on a global scale, for example, the GLAS (284,285), ATLID (286), and ESSP3-CENA (287) instruments, as well as ORACLE, (288) a proposed instrument to measure global ozone distribution. These space-based missions will complement existing ground-based systems by increasing global coverage. A new, ground-based, multitechnique lidar called ALOMAR (261) promises to provide measurements of air density, temperature, 3-D wind vector, momentum fluxes, aerosols, cloud particles, and selected trace gases at high vertical and temporal resolution.

The new millennium will bring synergistic combinations of space and ground-based radar and lidar facilities that will greatly enhance our ability to predict weather and climatic changes by making available measurements of wind, temperature, composition, and cloud properties.

ABBREVIATIONS AND ACRONYMS

ATLID	atmospheric lidar
ALOMAR	arctic lidar observatory for middle atmosphere research
AO	acousto-optic
CCD	charge coupled device
CNRS	centre national de la recherche scientifique

cw	continuous wave
DIAL	differential absorption lidar
DOAS	differential optical absorption spectroscopy
ESSP3	earth system science pathfinder 3
FOV	field-of-view
GLAS	geoscience laser altimeter system
Lidar	light detection and ranging
LITE	lidar in space technology experiment
LMT	liquid mirror telescope
MCP	micro channel plate
MCS	multichannel scaler
NASA	national aeronautics and space administration
Nd:YAG	neodymium:yttrium-aluminum garnet
ORACLE	ozone research with advanced cooperative lidar experiment
PCL	purple crow lidar
PMT	photomultiplier tube
PPRS	pure rotational raman lidar
PRF	pulse repetition frequency
RF	radio frequency
SIN	signal induced noise
SOR	starfire optical range
STS	space transport system
UT	Universal time

BIBLIOGRAPHY

- D. A. Leonard, B. Caputo, and F. E. Hoge, *Appl. Opt.* **18**, 1,732–1,745 (1979).
- J. L. Irish and T. E. White, *Coast. Eng.* **35**, 47–71 (1998).
- R. Barbini et al., *ICES J. Mar. Sci.* **55**, 793–802 (1998).
- I. M. Levin and K. S. Shifrin, *Remote Sensing Environ.* **65**, 105–111 (1998).
- J. H. Churnside, V. V. Tatarskii, and J. J. Wilson, *Appl. Opt.* **37**, 3,105–3,112 (1998).
- N. S. Higdon et al., *Proc. Nineteenth ILRC*, NASA, Hampton, Va., 1998, p. 651.
- D. R. Alexander, M. L. Rohlf, and J. C. Stauffer, *Proc. SPIE* **3,082**, 22–29 (1997).
- G. Klauber, C. Sini, P. M. Brinegar II, and M. M. Williams, *Proc. SPIE* **3,082**, 92–103 (1997).
- R. A. Mendonsa, *Photon Spectra* **31**, 20 (1997).
- [ANON], *Laser Focus World* **32**, 13 (1996).
- W. B. Scott, *Aviat. Week Space Technol.* **143**, 44 (1995).
- B. T. N. Evans, E. Yee, G. Roy, and J. Ho, *J. Aerosol Sci.* **25**, 1,549–1,566 (1994).
- A. V. Jelalian, W. H. Keene, and E. F. Pearson, in D. K. Killinger and A. Mooradian, eds., *Optical and Laser Remote Sensing*, Springer-Verlag, Berlin, 1983, pp. 341–349.
- www.bushnell.com.
- www.leica-camera.com.
- U. N. Singh, in *Optical Measurement Techniques and Application*, P. K. Rastogi, ed., Artech House, Norwood, MA, 1997, pp. 369–396.
- C. Weitkamp, in *Radiation and Water in the Climate System*, E. Raschke, ed., Springer-Verlag, Berlin, Germany, 1996, pp. 217–247.
- D. K. Killinger and A. Mooradian, eds., *Optical and Laser Remote Sensing*, Springer-Verlag, Berlin, 1983.
- L. Thomas, in *Spectroscopy in Environmental Science*, R. J. H. Clark and R. E. Hester, eds., Wiley, Chichester, England, 1995, pp. 1–47.
- R. Frehlich, in *Trends in Optics: Research, Development and Applications*, A. Consortini, ed., Academic Press, London, England, 1996, pp. 351–370.
- W. B. Grant, in *Tunable Laser Applications*, F. J. Duarte, ed., Marcel Dekker, NY, 1995, pp. 213–305.
- R. M. Measures, *Laser Remote Sensing: Fundamentals and Applications*, John Wiley & Sons, Inc., New York, NY, 1984.
- E. H. Synge, *Philos. Mag.* **52**, 1,014–1,020 (1930).
- Duclaux, *J. Phys. Radiat.* **7**, 361 (1936).
- E. O. Hulbert, *J. Opt. Soc. Am.* **27**, 377–382 (1937).
- R. Bureau, *Meteorologie* **3**, 292 (1946).
- L. Elterman, *J. Geophys. Res.* **58**, 519–530 (1953).
- S. S. Friedland, J. Katzenstein, and M. R. Zatzick, *J. Geophys. Res.* **61**, 415–434 (1956).
- T. H. Maiman, *Nature* **187**, 493 (1960).
- F. J. McClung and R. W. Hellworth, *J. Appl. Phys.* **33**, 828–829 (1962).
- L. D. Smullins and G. Fiocco, *Nature* **194**, 1,267 (1962).
- G. Fiocco and L. D. Smullins, *Nature* **199**, 1,275–1,276 (1963).
- H. Chen et al., *Opt. Lett.* **21**, 1,093–1,095 (1997).
- S. E. Bisson, J. E. M. Goldsmith, and M. G. Mitchell, *Appl. Opt.* **38**, 1,841–1,849 (1999).
- D. Rees, U. von Zahn et al., *Adv. Space Res.* **26**, 893–902 (2000).
- J. D. Spinhirne, *IEEE Trans. Geosci. Remote* **31**, 48 (1993).
- C. Nagasawa et al., *Appl. Opt.* **29**, 1,466–1,470 (1990).
- Y. Emery and C. Flesia, *Appl. Opt.* **37**, 2,238–2,241 (1998).
- R. J. Sica et al., *Appl. Opt.* **43**, 6,925–6,936 (1995).
- C. S. Gardner and W. M. Yang, *J. Geophys. Res.* **103**, 8,699–8,713 (1998).
- E. F. Borra and S. Thibault, *Photon Spectra* **32**, 142–146 (1998).
- G. V. Guerra et al., *J. Geophys. Res.* **104**, 22,287–22,292 (1999).
- D. M. Chambers and G. P. Nordin, *J. Opt. Soc. Am.* **16**, 1,184–1,193 (1999).
- <http://control.cass.usu.edu/lidar/index.htm>.
- S. Ishii et al., *Rev. Sci. Instrum.* **67**, 3,270–3,273 (1996).
- J. L. Baray et al., *Appl. Opt.* **38**, 6,808–6,817 (1999).
- K. W. Fischer et al., *Opt. Eng.* **34**, 499–511 (1995).
- Z. L. Hu et al., *Opt. Commun.* **156**, 289–293 (1998).
- J. A. McKay, *Appl. Opt.* **38**, 5,851–5,858 (1999).
- G. Beneditti-Michelangeli, F. Congeduti, and G. Fiocco, *JAS* **29**, 906–910 (1972).
- V. J. Abreu, J. E. Barnes, and P. B. Hays, *Appl. Opt.* **31**, 4,509–4,514 (1992).
- S. T. Shipley et al., *Appl. Opt.* **22**, 3,716–3,724 (1983).
- G. Fiocco and J. B. DeWolf, *JAS* **25**, 488–496 (1968).
- M. L. Chanin et al., *J. Geophys. Res.* **16**, 1,273–1,276 (1989).
- A. I. Carswell, in D. K. Killinger and A. Mooradian, eds., *Optical and Laser Remote Sensing*, Springer-Verlag, Berlin, 1983, pp. 318–326.
- K. Sassen, R. P. Benson, and J. D. Spinhirne, *Geophys. Res. Lett.* **27**, 673–676 (2000).
- G. P. Gobbi, *Appl. Opt.* **37**, 5,505–5,508 (1998).
- F. Cairo et al., *Appl. Opt.* **38**, 4,425–4,432 (1999).
- F. Cairo et al., *Rev. Sci. Instrum.* **67**, 3,274–3,280 (1996).
- J. P. Thayer et al., *Opt. Eng.* **36**, 2,045–2,061 (1997).

61. P. S. Argall and F. Jacka, *Appl. Opt.* **35**, 2,619–2,629 (1996).
62. F. L. Pedrotti and L. S. Pedrotti, *Introduction to Optics*, 2nd ed., Prentice-Hall, Englewood Cliffs, NJ, 1993, pp. 24–25.
63. E. L. Dereniak and D. G. Crowe, *Optical Radiation Detectors*, John Wiley & Sons, Inc., New York, NY, 1984, pp. 116–121.
64. M. J. McGill and W. R. Skinner, *Opt. Eng.* **36**, 139–145 (1997).
65. W. C. Priedhorsky, R. C. Smith, and C. Ho, *Appl. Opt.* **35**, 441–452 (1996).
66. T. Erikson et al., *Appl. Opt.* **38**, 2,605–2,613 (1999).
67. N. S. Higdon et al., *Appl. Opt.* **33**, 6,422–6,438 (1994).
68. M. Wu et al., *Appl. Spectrosc.* **54**, 800–806 (2000).
69. A. M. South, I. M. Povey, and R. L. Jones, *J. Geophys. Res.* **103**, 31,191–31,202 (1998).
70. R. W. Engstrom, *Photomultiplier Handbook*, RCA Corporation, USA, 1980.
71. J. Wilson and J. F. B. Hawkes, *Optoelectronics, An Introduction*, 2nd ed., Prentice-Hall, Cambridge, 1989, pp. 265–270.
72. D. P. Donovan, J. A. Whiteway, and A. I. Carswell, *Appl. Opt.* **32**, 6,742–6,753 (1993).
73. A. O. Langford, *Appl. Opt.* **34**, 8,330–8,340 (1995).
74. M. P. Bristow, D. H. Bundy, and A. G. Wright, *Appl. Opt.* **34**, 4,437–4,452 (1995).
75. Y. Z. Zhao, *Appl. Opt.* **38**, 4,639–4,648 (1999).
76. C. K. Williamson and R. J. De Young, *Appl. Opt.* **39**, 1,973–1,979 (2000).
77. J. M. Vaughan, *Phys. Scripta* **T78**, 73–81 (1998).
78. R. M. Huffaker and P. A. Reveley, *Pure Appl. Opt.* **7**, 863–873 (1998).
79. R. Targ et al., *Appl. Opt.* **35**, 7,117–7,127 (1996).
80. R. M. Huffaker and R. M. Hardesty, *Proc. IEEE* **84**, 181–204 (1996).
81. S. M. Hannon and J. A. Thomson, *J. Mod. Opt.* **41**, 2,175–2,196 (1994).
82. V. M. Gordienko et al., *Opt. Eng.* **33**, 3,206–3,213 (1994).
83. P. S. Argall et al., *Appl. Opt.* **39**, 2,393–2,400 (2000).
84. A. Ben-David, *Appl. Opt.* **38**, 2,616–2,624 (1999).
85. Y. J. Park, S. W. Dho, and H. J. Kong, *Appl. Opt.* **36**, 5,158–5,161 (1997).
86. K. L. Coulson, *Solar and Terrestrial Radiation*, Academic Press, NY, 1975.
87. E. J. McCartney, *Optics of the Atmosphere*, John Wiley & Sons, Inc., New York, NY, 1976.
88. P. N. Slater, *Remote Sensing, Optics and Optical Systems*, Addison-Wesley, Toronto, 1980.
89. V. V. Sobolev, *Light Scattering in Planetary Atmospheres*, Pergamon Press, Oxford, 1975.
90. G. Mie, *Ann. Physik* **25**, 377–445 (1908).
91. D. Muller et al., *Appl. Opt.* **39**, 1,879–1,892 (2000).
92. J. P. Diaz et al., *J. Geophys. Res.* **105**, 4,979–4,991 (2000).
93. F. Masci, *Ann. Geofis.* **42**, 71–83 (1999).
94. D. Muller, U. Wandinger, and A. Ansmann, *Appl. Opt.* **38**, 2,358–2,368 (1999).
95. C. Erlick and J. E. Frederick, *J. Geophys. Res.* **103**, 23,275–23,285 (1998).
96. I. N. Sokolik, O. B. Toon, and R. W. Bergstrom, *J. Geophys. Res.* **103**, 8,813–8,826 (1998).
97. A. A. Kokhanovsky, *J. Atmos. Sci.* **55**, 314–320 (1998).
98. W. C. Conant, *J. Geophys. Res.* **105**, 15,347–15,360 (2000).
99. G. M. McFarquhar et al., *J. Atmos. Sci.* **57**, 1,841–1,853 (2000).
100. R. M. Hoff et al., *J. Geophys. Res.* **101**, 19,199–19,209 (1996).
101. J. L. Brenguier et al., *Tellus B* **52**, 815–827 (2000).
102. J. Redemann et al., *J. Geophys. Res.* **105**, 9,949–9,970 (2000).
103. M. Minomura et al., *Adv. Space Res.* **25**, 1,033–1,036 (2000).
104. A. T. Young, *Appl. Opt.* **19**, 3,427–3,428 (1980).
105. A. T. Young, *J. Appl. Meteorol.* **20**, 328–330 (1981).
106. A. T. Young, *Phys. Today* **35**, 42–48 (1982).
107. Rayleigh (J. W. Strutt), *Philos. Mag.* **41**, 274–279 (1871).
108. Rayleigh (J. W. Strutt), *Philos. Mag.* **41**, 447–454 (1871).
109. Rayleigh (J. W. Strutt), *Philos. Mag.* **12**, 81 (1881).
110. Rayleigh (J. W. Strutt), *Philos. Mag.* **47**, 375–384 (1899).
111. J. A. Stratton, *Electromagnetic Theory*, McGraw-Hill, NY, 1941.
112. M. Kerker, *The Scattering of Light and Electromagnetic Radiation*, Academic Press, NY, 1969.
113. R. Penndorf, *J. Opt. Soc. Am.* **52**, 402–408 (1962).
114. W. E. K. Middleton, *Vision Through the Atmosphere*, University of Toronto Press, Toronto, 1952.
115. M. Born and E. Wolf, *Principles of Optics*, Pergamon Press, Great Britain, Oxford, 1970.
116. G. S. Kent and R. W. H. Wright, *J. Atmos. Terrestrial Phys.* **32**, 917–943 (1970).
117. R. T. H. Collis and P. B. Russell, in E. D. Hinkley, ed., *Laser Monitoring of the Atmosphere*, Springer-Verlag, Berlin, 1976.
118. G. Fiocco, in R. A. Vincent, ed., *Handbook for MAP*, vol. 13, ICSU, SCOSTEP, Urbana, IL, 1984.
119. G. Fiocco et al., *Nature* **229**, 79–80 (1971).
120. A. Hauchecorne and M. L. Chanin, *Geophys. Res. Lett.* **7**, 565–568 (1980).
121. T. Shibata, M. Kobuchi, and M. Maeda, *Appl. Opt.* **25**, 685–688 (1986).
122. C. O. Hines, *Can. J. Phys.* **38**, 1,441–1,481 (1960).
123. R. J. Sica and M. D. Thorsley, *Geophys. Res. Lett.* **23**, 2,797–2,800 (1996).
124. T. J. Duck, J. A. Whiteway, and I. A. Carswell, *J. Geophys. Res.* **105**, 22,909–22,918 (2000).
125. T. Leblanc et al., *J. Geophys. Res.* **103**, 17,191–17,204 (1998).
126. M. L. Chanin and A. Hauchecorne, *J. Geophys. Res.* **86**, 9,715–9,721 (1981).
127. M. L. Chanin and A. Hauchecorne, in R. A. Vincent, ed., *Handbook for MAP*, vol. 13, ICSU, SCOSTEP, Urbana, IL, 1984, pp. 87–98.
128. M. L. Chanin, N. Squires, and A. Hauchecorne, *J. Geophys. Res.* **92**, 10,933–10,941 (1987).
129. C. S. Gardner, M. S. Miller, and C. H. Liu, *J. Atmos. Sci.* **46**, 1,838–1,854 (1989).
130. T. J. Beatty, C. A. Hostetler, and C. S. Gardner, *J. Atmos. Sci.* **49**, 477–496 (1992).
131. A. I. Carswell et al., *Can. J. Phys.* **69**, 1,076 (1991).
132. M. M. Mwangi, R. J. Sica, and P. S. Argall, *J. Geophys. Res.* **106**, 10,313 (2001).
133. R. J. States and C. S. Gardner, *J. Geophys. Res.* **104**, 11,783–11,798 (1999).
134. E. A. Hylleraas, *Mathematical and Theoretical Physics*, John Wiley & Sons, Inc., New York, NY, 1970.

135. E. H. Kennard, *Kinetic Theory of Gases*, McGraw-Hill, NY, 1938.
136. C. A. Tepley, S. I. Sargoytchev, and R. Rojas, *IEEE Trans. Geosci. Remote Sensing* **31**, 36–47 (1993).
137. C. Souprayen et al., *Appl. Opt.* **38**, 2,410–2,421 (1999).
138. H. C. Van de Hulst, *Light Scattering by Small Particles*, John Wiley & Sons, Inc., New York, NY, 1951.
139. C. E. Bohren and D. R. Huffman, *Absorption and Scattering of Light by Small Particles*, John Wiley & Sons, Inc., New York, NY, 1983.
140. L. P. Bayvel and A. R. Jones, *Electromagnetic Scattering and its Applications*, Applied Science, England, London, 1981.
141. C. N. Davies, *J. Aerosol. Sci.* **18**, 469–477 (1987).
142. L. G. Yaskovich, *Izvestiya, Atmos. Oceanic Phys.* **22**, 640–645 (1986).
143. Y. S. Georgiyevskiy et al., *Izvestiya, Atmos. Oceanic Phys.* **22**, 646–651 (1986).
144. J. Rosen et al., *J. Geophys. Res.* **105**, 17,833–17,842 (2000).
145. A. Ansmann et al., *Geophys. Res. Lett.* **27**, 964–966 (2000).
146. T. Sakai et al., *Atmos. Environ.* **34**, 431–442 (2000).
147. M. A. Fenn et al., *J. Geophys. Res.* **104**, 16,197–16,212 (1999).
148. R. A. Ferrare et al., *J. Geophys. Res.* **103**, 19,673–19,689 (1998).
149. C. E. Junge, *Air Chemistry and Radioactivity*, Academic Press, NY, 1963.
150. G. Di Donfrancesco et al., *J. Atmos. Sol-Terrestrial Phys.* **62**, 713–723 (2000).
151. D. Guzzi et al., *Geophys. Res. Lett.* **26**, 2,199–2,202 (1999).
152. V. V. Zuev, V. D. Burlakov, and A. V. El'nikov, *J. Aerosol Sci.* **103**, 13,873–13,891 (1998).
153. A. di Sarra et al., *J. Geophys. Res.* **103**, 13,873–13,891 (1998).
154. G. S. Kent and G. M. Hansen, *Appl. Opt.* **37**, 3,861–3,872 (1998).
155. M. H. Bergin et al., *J. Geophys. Res.* **105**, 6,807–6,816 (2000).
156. R. A. Ferrare et al., *J. Geophys. Res.* **103**, 19,663–19,672 (1998).
157. C. M. R. Platt et al., *J. Atmos. Sci.* **55**, 1,977–1,996 (1998).
158. A. Robock, *Rev. Geophys.* **38**, 191–219 (2000).
159. W. T. Hyde and T. J. Crowley, *J. Climate* **13**, 1,445–1,450 (2000).
160. H. Kuhnert et al., *Int. J. Earth Sci.* **88**, 725–732 (2000).
161. C. J. Grund and E. W. Eloranta, *Opt. Eng.* **30**, 6–12 (1991).
162. C. Y. She et al., *Appl. Opt.* **31**, 2,095–2,106 (1992).
163. D. P. Donovan et al., *Geophys. Res. Lett.* **25**, 3,139–3,142 (1998).
164. Y. Sasano and E. V. Browell, *Appl. Opt.* **28**, 1,670–1,679 (1989).
165. D. Muller et al., *Geophys. Res. Lett.* **27**, 1,403–1,406 (2000).
166. G. Beyerle et al., *Geophys. Res. Lett.* **25**, 919–922 (1998).
167. M. J. Post et al., *J. Geophys. Res.* **102**, 13,535–13,542 (1997).
168. J. D. Spinhirne et al., *Appl. Opt.* **36**, 3,475–3,490 (1997).
169. T. Murayama et al., *J. Geophys. Res.* **104**, 3,1781–3,1792 (1999).
170. G. Roy et al., *Appl. Opt.* **38**, 5,202–5,211 (1999).
171. K. Sassen K and C. Y. Hsueh, *Geophys. Res. Lett.* **25**, 1,165–1,168 (1998).
172. T. Murayama et al., *J. Meteorol. Soc. Jpn.* **74**, 571–578 (1996).
173. K. Sassen, *Bull. Am. Meteorol. Soc.* **72**, 1,848–1,866 (1991).
174. G. A. Reagan, J. D. Spinhirne, and M. P. McCormick, *Proc. IEEE* **77**, 433–448 (1989).
175. D. P. Donovan et al., *Geophys. Res. Lett.* **24**, 2,709–2,712 (1997).
176. G. P. Gobbi, G. Di Donfrancesco, and A. Adriani, *J. Geophys. Res.* **103**, 10,859–10,873 (1998).
177. M. Pantani et al., *J. Aerosol. Sci.* **30**, 559–567 (1999).
178. H. Mehrtens et al., *Geophys. Res. Lett.* **26**, 603–606 (1999).
179. T. Shibata et al., *J. Geophys. Res.* **104**, 21,603–21,611 (1999).
180. A. Tsias et al., *J. Geophys. Res.* **104**, 23,961–23,969 (1999).
181. F. Stefanutti et al., *Appl. Phys.* **B55**, 13–17 (1992).
182. K. S. Carslaw et al., *Nature* **391**, 675–678 (1998).
183. B. M. Knudsen et al., *Geophys. Res. Lett.* **25**, 627–630 (1998).
184. I. A. MacKenzie and R. S. Harwood, *J. Geophys. Res.* **105**, 9,033–9,051 (2000).
185. <http://oea.larc.nasa.gov/PAIS/LITE.html>.
186. D. M. Winker, R. H. Couch, and M. P. McCormick, *Proc. IEEE* **84**, 164–180 (1996).
187. L. O'Connor, *Mech. Eng.* **117**, 77–79 (1995).
188. K. B. Strawbridge and R. M. Hoff, *Geophys. Res. Lett.* **23**, 73–76 (1996).
189. Y. Y. Y. Gu et al., *Appl. Opt.* **36**, 5,148–5,157 (1997).
190. V. Cuomo et al., *J. Geophys. Res.* **103**, 11,455–11,464 (1998).
191. H. Shimizu, S. A. Lee, and C. Y. She, *Appl. Opt.* **22**, 1,373–1,382 (1983).
192. R. M. Hardesty, in D. K. Killinger and A. Mooradian, eds., *Optical and Laser Remote Sensing*, Springer-Verlag, Berlin, 1983.
193. S. D. Mayor et al., *J. Atmos. Ocean. Tech.* **14**, 1,110–1,126 (1997).
194. J. Bilbro, in D. K. Killinger and A. Mooradian, eds., *Optical and Laser Remote Sensing*, Springer-Verlag, Berlin, 1983.
195. J. Rothermel et al., *Opt. Express* **2**, 40–50 (1998).
196. J. Rothermel et al., *Bull. Am. Meteorol. Soc.* **79**, 581–599 (1998).
197. R. Frehlich, *J. Appl. Meteorol.* **39**, 245–262 (2000).
198. R. M. Schotland, *Proc. 3rd Symp. Remote Sensing Environ.*, 1964, pp. 215–224.
199. R. M. Schotland, *Proc. 4th Symp. Remote Sensing Environ.*, 1966, pp. 273–283.
200. D. K. Killinger and N. Menyuk, *Science* **235**, 37–45 (1987).
201. K. W. Rothe, U. Brinkmann, and H. Walther, *Appl. Phys.* **3**, 115 (1974).
202. N. Menyuk, D. K. Killinger, and W. E. DeFeo, in D. K. Killinger and A. Mooradian, eds., *Optical and Laser Remote Sensing*, Springer-Verlag, Berlin, 1983.
203. E. E. Uthe, *Appl. Opt.* **25**, 2,492–2,498 (1986).
204. E. Zanzottera, *Crit. Rev. Anal. Chem.* **21**, 279 (1990).
205. M. Pinandito et al., *Opt. Rev.* **5**, 252–256 (1998).
206. R. Toriumi et al., *Jpn. J. Appl. Phys.* **38**, 6,372–6,378 (1999).
207. R. Toriumi, H. Tai, and N. Takeuchi, *Opt. Eng.* **35**, 2,371–2,375 (1996).
208. D. Kim et al., *J. Korean Phys. Soc.* **30**, 458–462 (1997).
209. V. Wulfmeyer, *J. Atmos. Sci.* **56**, 1,055–1,076 (1999).
210. A. Fix, V. Weiss, and G. Ehret, *Pure Appl. Opt.* **7**, 837–852 (1998).

211. E. V. Browell, *Proc. IEEE* **77**, 419–432 (1989).
212. R. M. Banta et al., *J. Geophys. Res.* **103**, 22,519–22,544 (1998).
213. E. Durieux et al., *Atmos. Environ.* **32**, 2,141–2,150 (1998).
214. P. Weibring et al., *Appl. Phys. B* **67**, 419–426 (1998).
215. T. Fukuchi et al., *Opt. Eng.* **38**, 141–145 (1999).
216. N. S. Prasad and A. R. Geiger, *Opt. Eng.* **35**, 1,105–1,111 (1996).
217. M. J. T. Milton et al., *Opt. Commun.* **142**, 153–160 (1997).
218. K. Ikuta et al., *Jpn. J. Appl. Phys.* **38**, 110–114 (1999).
219. J. E. Kalshoven et al., *Appl. Opt.* **20**, 1,967–1,971 (1981).
220. G. K. Schwemmer et al., *Rev. Sci. Instrum.* **58**, 2,226–2,237 (1987).
221. V. Wulfmeyer, *Appl. Opt.* **37**, 3,804–3,824 (1998).
222. J. Pelon, S. Godin, and G. Megie, *J. Geophys. Res.* **91**, 8,667–8,671 (1986).
223. J. Werner, K. W. Rothe, and H. Walther, *Appl. Phys., Ser. B* **32**, 113 (1983).
224. I. S. McDermid, S. M. Godin, and L. O. Lindqvist, *Appl. Opt.* **29**, 3,603–3,612 (1990).
225. T. J. McGee et al., *Opt. Eng.* **30**, 31–39 (1991).
226. T. Leblanc and I. S. McDermid, *J. Geophys. Res.* **105**, 14,613–14,623 (2000).
227. W. B. Grant et al., *Geophys. Res. Lett.* **25**, 623–626 (1998).
228. T. J. McGee et al., *Opt. Eng.* **34**, 1,421–1,430 (1995).
229. J. R. Quagliano et al., *Appl. Opt.* **36**, 1,915–1,927 (1997).
230. C. Bellecci and F. De Donato, *Appl. Opt.* **38**, 5,212–5,217 (1999).
231. G. Herzberg, *Molecular Spectra and Molecular Structure I. Spectra of Diatomic Molecules*, 2nd ed., Van Nostrand Reinhold Company, NY, 1950.
232. C. V. Raman, *Indian J. Phys.* **2**, 387 (1928).
233. J. A. Cooney, *Appl. Phys. Lett.* **12**, 40–42 (1968).
234. D. A. Leonard, *Nature* **216**, 142–143 (1967).
235. J. A. Cooney, *J. Appl. Meteorol.* **9**, 182 (1970).
236. J. A. Cooney, *J. Geophys. Res.* **77**, 1,078 (1972).
237. J. A. Cooney, K. Petri, and A. Salik, *Appl. Opt.* **24**, 104–108 (1985).
238. S. H. Melfi, *Appl. Opt.* **11**, 1,605 (1972).
239. V. Sherlock et al., *Appl. Opt.* **38**, 5,838–5,850 (1999).
240. W. E. Eichinger et al., *J. Atmos. Oceanic Technol.* **16**, 1,753–1,766 (1999).
241. S. H. Melfi et al., *Appl. Opt.* **36**, 3,551–3,559 (1997).
242. D. N. Whiteman and S. H. Melfi, *J. Geophys. Res.* **104**, 31,411–31,419 (1999).
243. B. Demoz et al., *Geophys. Res. Lett.* **27**, 1,899–1,902 (2000).
244. A. Ansmann et al., *J. Atmos. Sci.* **54**, 2,630–2,641 (1997).
245. R. Ferrare et al., *J. Geophys. Res.* **105**, 9,935–9,947 (2000).
246. P. Keckhut, M. L. Chanin, and A. Hauchecorne, *Appl. Opt.* **29**, 5,182–5,186 (1990).
247. K. D. Evans et al., *Appl. Opt.* **36**, 2,594–2,602 (1997).
248. M. R. Gross et al., *Appl. Opt.* **36**, 5,987–5,995 (1997).
249. J. A. Cooney, *J. Appl. Meteorol.* **11**, 108–112 (1972).
250. A. Cohen, J. A. Cooney, and K. N. Geller, *Appl. Opt.* **15**, 2,896 (1976).
251. J. A. Cooney and M. Pina, *Appl. Opt.* **15**, 602 (1976).
252. R. Gill et al., *Izvestiya, Atmos. Oceanic Phys.* **22**, 646–651 (1979).
253. Yu. F. Arshinov et al., *Appl. Opt.* **22**, 2,984–2,990 (1983).
254. Yu. F. Arshinov and S. M. Bobrovnikov, *Appl. Opt.* **38**, 4,635–4,638 (1999).
255. A. Behrendt and J. Reichardt, *Appl. Opt.* **39**, 1,372–1,378 (2000).
256. J. W. Chamberlain, *Physics of Aurora and Airglow*, Academic Press, NY, 1961.
257. J. M. C. Plane, R. M. Cox, and R. J. Rollason, *Adv. Space Res.* **24**, 1,559–1,570 (1999).
258. V. W. J. H. Kirchhoff et al., *J. Geophys. Res.* **91**, 13,303–13,307 (1986).
259. B. R. Clemesha et al., *Geophys. Res. Lett.* **26**, 1,681–1,684 (1999).
260. K. H. Fricke and U. von Zahn, *J. Atmos. Terrestrial Phys.* **47**, 499–512 (1985).
261. U. von Zahn et al., *Ann. Geophys.-Atmos. Hydr.* **18**, 815–833 (2000).
262. C. S. Gardner et al., *J. Geophys. Res.* **91**, 13,659–13,673 (1986).
263. X. Z. Chu et al., *Geophys. Res. Lett.* **27**, 1,815–1,818 (2000).
264. A. Nomura et al., *Geophys. Res. Lett.* **14**, 700–703 (1987).
265. C. Y. She et al., *Geophys. Res. Lett.* **22**, 377–380 (1995).
266. M. R. Bowman, A. J. Gibson, and M. C. W. Sandford, *Nature* **221**, 456–457 (1969).
267. D. M. Hunten, *Space Sci. Rev.* **6**, 493 (1967).
268. A. Gibson, L. Thomas, and S. Bhattachacharyya, *Nature* **281**, 131–132 (1979).
269. K. H. Frick and U. von Zahn, *J. Atmos. Terrestrial Phys.* **47**, 499–512 (1985).
270. G. C. Papen, W. M. Pfenninger, and D. M. Simonich, *Appl. Opt.* **34**, 480–498 (1995).
271. C. Y. She et al., *Geophys. Res. Lett.* **17**, 929–932 (1990).
272. C. Y. She and J. R. Yu, *Geophys. Res. Lett.* **21**, 1,771–1,774 (1994).
273. R. E. Bills, C. S. Gardner, and C. Y. She, *Opt. Eng.* **30**, 13–21 (1991).
274. C. Granier, J. P. Jegou, and G. Megie, *Proc. 12th Int. Laser Radar Conf.*, Aix en Provence, France, 1984, pp. 229–232.
275. M. Alpers, J. Hoffner, and U. von Zahn, *Geophys. Res. Lett.* **23**, 567–570 (1996).
276. G. C. Papen, C. S. Gardner, and W. M. Pfenninger, *Appl. Opt.* **34**, 6,950–6,958 (1995).
277. V. Eska, U. von Zahn, and J. M. C. Plane, *J. Geophys. Res.* **104**, 17,173–17,186 (1999).
278. J. P. Jegou et al., *Geophys. Res. Lett.* **7**, 995–998 (1980).
279. B. R. Clemesha, *MAP Handbook* **13**, 99–112 (1984).
280. J. A. Gelbwachs, *Appl. Opt.* **33**, 7,151–7,156 (1994).
281. X. Z. Chu et al., *Geophys. Res. Lett.* **27**, 1,807–1,810 (2000).
282. L. Thomas, *Phil. Trans. R. Soc. Lond. Ser. A* **323**, 597–609 (1987).
283. U. von Zahn and J. Hoffner, *Geophys. Res. Lett.* **23**, 141–144 (1996).
284. J. D. Spinhirne and S. P. Palm, *18th Int. Laser Radar Conf. (ILRC)*, Springer-Verlag, 1996, pp. 213–216.
285. <http://virl.gsfc.nasa.gov/glas/index.html>.
286. A. E. Marini, *ESA Bull.-Eur. Space* **95**, 113–118 (1998).
287. <http://essp.gsfc.nasa.gov/cena/index.html>.
288. <http://aesd.larc.nasa.gov/oracle/index.htm>.
289. S. Fleming et al., *Tech. Memoir*, NASA TM-100697, 1988.